Chromatin arranges in filaments of blobs with nanoscale functional zonation

E. Miron[1,2], R. Oldenkamp[1,2], D. M. S. Pinto[1], J. M. Brown[3], A. R. Carvalho Faria[1], H. A. Shaban[4], J. D. P. Rhodes[1], C. Innocent[1,5], S. de Ornellas[3], V. Buckle[3], L. Schermelleh[1]*

[1] Department of Biochemistry, University of Oxford, Oxford OX1 3QU, United Kingdom
[2] Current address: Division of gene regulation, Netherlands Cancer Institute, Plesmanlaan 121, 1066 CX Amsterdam, the Netherlands
[3] MRC Weatherall Institute of Molecular Medicine, Haematology Unit, University of Oxford, Oxford OX3 9DS, United Kingdom
[4] Spectroscopy Department, Physics Division, National Research Centre, 12622 Dokki, Cairo, Egypt
[5] Current address: Neurology Department, Harvard Medical School, Boston Children's Hospital, 300 Longwood Ave, Boston MA 02115

*Correspondence should be addressed to L.S. (lothar.schermelleh@bioch.ox.ac.uk)

Keywords: Chromatin, TAD, epigenome, nuclear organization, quantitative image analysis, super-resolution microscopy, structured illumination microscopy, 3D-SIM

Three-dimensional (3D) chromatin organisation plays a key role in regulating genome function in higher eukaryotes. Despite recognition that the genome partitions into ~1Mb-sized topological associated domains (TADs) based on ensemble Hi-C measurements, many features of the physical organisation at the single cell level remain underexplored. Using 3D super-resolution microscopy, we reveal a sequential curvilinear arrangement of globular chromatin domains with viscoelastic properties ('blobs') juxtaposed to an RNA-populated interchromatin (IC) network. Quantitative mapping of genome function markers uncovers a zonal distribution, with RNA-binding factors concentrated in the IC, confinement of structural proteins and transcriptionally active/permissive marks to chromatin domain surfaces, and enrichment of repressive marks towards the interior. This correlation between nanoscale topology and genome function is relaxed in postreplicative chromatin, accentuated in replicative senescence, persists upon ATP depletion and hyperosmolarity induced chromatin condensation and, remarkably, after inactivation of cohesin. Our findings support a model of a higher-order chromatin architecture on the size level of TADs that creates and modulates distinct functional environments through a combination of biophysical parameters such as density and ATP-driven processes such as replication and transcription, but independent of cohesin.

The genome in mammalian cell nuclei is hierarchically organised at various size scales that correlate with diverse genomic functions[1,2]. At the base pair to kilobase pair level, DNA is wrapped around core histones to create nucleosomes that form the building blocks of chromatin[3]. At the 100 Mb scale, whole chromosomes harbour distinct territories within the nucleus with transcriptionally active euchromatic and inactive heterochromatic segments tending to segregate into specific nuclear sub-regions[4]. The intermediate chromatin organization ranging from several kb to 100 Mb still remains poorly understood[5]. Advances in next-generation sequencing based chromosome conformation capturing methods (3C/Hi-C) have revealed a genomic landscape composed of ~400 kb to ~1 Mb-sized topologically associating domains (TADs)[6,7]. TADs are genomic regions which have elevated intra-TAD interaction relative to sequences outside TADs; deletion of TAD boundaries leads to aberrant reprogramming of the transcriptome[8]. Chromatin immunoprecipitation sequencing (ChIP-Seq) identified the CCCTC-binding factor (CTCF) as a key regulator in TAD organisation, binding to convergently oriented recognition sequences which flank TADs and thus define their boundaries at the linear scale[9]. Although the exact mechanisms of TAD formation and maintenance has yet to be elucidated, co-occurrence of the ring-shaped

cohesin complex at CTCF binding sites suggest a regulatory role of cohesin in shaping TAD structures through chromatin loop extrusion[10–13]. Accordingly, loss of cohesin function leads to an erasure of TAD signatures on Hi-C interaction maps[14].

Whereas the linear genomic size of TAD structures is well defined, their spatiotemporal organization is largely underexplored. Genomic-based methods such as Hi-C and ChIP-Seq are characterized by the need for averaging large cell populations to generate *in silico* models, thereby falling short in explaining the biophysical forces that maintain the 3D epigenome. Ensemble data result in semi-quantitative models that do not address cell to cell variability and lack information on the absolute structure and temporal dynamics of chromatin domains. In fact, single-cell Hi-C and more recent microscopy-based approaches observe variability in chromatin folding at the level of TAD topologies, highlighting a high degree of stochasticity and heterogeneity in chromatin conformations *in situ*[15–18]. Fluorescent *in situ* hybridization (FISH) of specific DNA regions has been a powerful tool in visualizing chromatin structures, revealing the appearance of TAD topologies as chromatin domains with a diameter of several hundred nanometres when imaged with super-resolution microscopy[17,19–21]. *In silico* simulations of chromatin as a melted polymer suggest that the charged properties of modified histone tails alter the compaction status of such chromatin domains[22], thereby explaining the increase in physical size of epigenetically active domains compared to epigenetically inactive domains[23]. It is further suggested that protein mobility is hampered with increasing chromatin density through physical hindrance, which may allow relative size differences between small transcription factors (TFs) and large nuclear macro-complexes such as the transcription machinery to be exploited as a mechanism of transcriptional control[24].

3D super-resolution chromatin imaging reveals a curvilinear filament of coherently moving globular domains, distinct from an RNA-occupied interchromatin network

The study of <1 Mb chromatin domain topologies in single cells *in situ* and *in vivo* have long been under-characterized in conventional microscopy studies, as their scales fall just beyond the diffraction limit of light. Advances in super-resolution microscopy now put such structures within spatial reach[17,21]. Super-resolution 3D structured illumination microscopy (3D-SIM) enables fast multicolour 3D acquisition of whole cells with 8-fold enhanced volumetric resolution and strongly enhanced contrast compared to conventional fluorescence microscopy[25]. Previous 3D-SIM studies resolved 4′,6-diamidino-2-phenylindole (DAPI)-stained chromatin in mammalian somatic cells as an intricate sponge-like structure, that is juxtaposed to channels of no detectable chromatin (the inter-chromatin compartment, IC)

which permeate throughout the nucleus, ending at nuclear pores[26–28]. Using data quality-controlled 3D-SIM (Methods; Extended Data Fig. 1a), we first confirmed the presence of this structural arrangement in mouse (C127) and human (Hela) somatic cell lines (Extended Data Fig. 1a-c). DNA staining with either DAPI or SYTOX Green after formaldehyde fixation revealed the same characteristic pattern of a convoluted filamentous chromatin structure and an interchromatin network (Extended Data Fig. 1b, left). Complementary 3D stimulated emission depletion (STED) microscopy of SYTOX-labelled C127 cells confirmed the topological features observed with 3D-SIM (Extended Data Fig. 1b, middle). Control experiments in HeLa cells stably expressing histone H2B-GFP showed a near, albeit not complete colocalisation of H2B-GFP and DNA staining, in line with a mixture of tagged and untagged H2B incorporated into chromatin[29] (Extended Data Fig. 1c).

To better understand the nature of the seemingly 'empty' IC network compartment we performed an extended 5-ethenyluridine (EU) pulse labelling and subsequent click chemistry to detect of all RNAs transcribed during the labelling period[30]. We observed a striking enrichment of bulk RNA in the IC space including nucleoli and nuclear pore channels, and almost mutual exclusion with DAPI-stained chromatin (Fig. 1a, b). Plotting a line profile through a representative region of euchromatin shows RNA-filled IC and chromatin features with minimal diameter of approx. 160 nm (Fig. 1c) up to several hundred nanometres in heterochromatic regions (data not shown).

Along with a visual comparison we applied an unbiased non-linear segmentation algorithm on the chromatin staining assigning each voxel in the nuclear space to one of seven relative intensity classes with the lowest (class 1) denoting the IC, and the other classes 2-7 denoting the chromatin compartment from low to high density (Methods, Extended Data Fig. 1d). Of the quantified nuclear volume (Extended Data Fig. 1c) ~30% was classified as IC network with subsequent decreasing proportions for lower to higher chromatin density (classes 2 to 7, Extended Data Fig. 1e). We further assessed the average diameter of the convoluted filamentous chromatin structure in C127 cells to be 350 nm (Extended Data Fig. 3, Methods); the value is proximate to the mid-point (330 nm) of the previous empirically observed ranges (Fig. 1c). To exclude fixation artefacts, we adopted our 3D-SIM acquisition scheme to enable fast live cell imaging of H2B-GFP expressing cells confirming the presence of a chromatin – interchromatin network *in vivo* (Extended Data Fig.1b, right). Time-lapse 3D-SIM imaging of HeLa H2B-GFP cells unveiled a highly dynamic behaviour of chromatin domain features over different observation periods and time intervals (Fig.1d, Extended Data Fig. 2a, Supplementary Movies 1-3).

Quantitative flow field analysis[31] (Methods; Fig. 1d, e; Supplementary Movie 4) reveals spatially coherent motion of chromatin (i.e. fields with same motion direction) with a correlation length of ~2.5 to 3 μm for time intervals between 2 s and >20 s, indicating a change in correlation length of 0.5 μm between adjacent coherently moving domains (Fig. 1e, middle). This is accompanied by smoother transitions between these domains for increasing time intervals (Fig. 1e, bottom). Mapping of chromatin dynamics using a Bayesian model selection approach demonstrates primarily slow diffusive and sub-diffusive dynamics (Extended Data Fig. 2b). These results are consistent with a viscoelastic properties of chromatin characterised by mechanical coupling and coherent motion of high-viscous droplet-like domains[31,32], best described as diffusive 'blobs'.

Next, we used DNA fluorescence *in situ* hybridization (FISH) detection to place the observed 3D chromatin landscape in the context of TADs as defined by Hi-C experiments. Conventional DNA-FISH protocols require heat denaturation which disrupts chromatin structures below ~1-Mb-size levels[33]. To overcome this potential problem, we have implemented a non-denaturing FISH method, termed resolution after single-stranded exonuclease resection (RASER)-FISH[34], in order to faithfully preserve chromatin ultrastructure. We applied RASER-FISH to study the topology of a previously characterized TAD (0.7 Mb TAD H) located on the mouse X chromosome[19] (Fig. 1f, Extended Data Fig. 4a). Quantitative analysis of 21 TAD H RASER-FISH signals from active (non-Barr body) X chromosomes revealed an average core diameter of 350 nm. Although most TADs in single cells display a globular shape they are not uniform spheres but extend in at least one dimension to a maximum extension of 500 nm as confirmed by a standard deviation between all TADs (Fig. 1g, Extended Data Fig. 4b). Importantly, TAD FISH signals coincide with the underlying chromatin density stained by DAPI (Fig. 1f). Furthermore, multi-colour RASER-FISH of neighbouring domains spanning the α-globin locus revealed a curvilinear path, where each domain is a discrete blob within the convoluted filament (Fig. 1h, Extended Data Fig. 4c).

We conclude that chromatin in somatic interphase cells arranges as a convoluted curvilinear filament partitioned into discrete globular or extended chromatin blobs. These can accommodate TADs in a range of chromatin densities and form physical viscoelastic entities with constrained local dynamics that are separated from a DNA-free, RNA-occupied interchromatin network space.

Functional marker distribution reveal nanoscale 3D zonation

Previous studies correlating Hi-C-based TAD distributions with ChIP-seq mapping of histone post translational modifications (PTMs) and chromatin factors along the linear (1D) genome highlighted an enrichment for cohesin and CTCF at the TAD boundaries[7]. Drawing from our own previous study of non-random localization of active and silenced chromatin histone PTMs[27,28], we undertook to systematically map genomic function against the observed chromatin blob filament – IC network. To this end we have devised a pipeline (Cha*i*N, Chain high-throughput analysis of the *in situ* Nucleome), Extended Data Fig. 5 and Methods for details) for automated high-throughput image analysis, that allows mining spatial high-content information from thousands of multicolour-labelled 3D-SIM nuclear volume datasets after applying SIM optimized immunofluorescence (IF) labelling protocols[36] (Methods). Cha*i*N classifies the chromatin signal into class 1 if no signal detected (the IC), classes 2 and 3 confined to the outer fringes of the blob filament, classes 4 and 5 denote the interior of blobs and classes 6 and 7 primarily denoting densely packed constitutive heterochromatin regions[28]. (Fig. 2a). We characterised the 3D epigenome landscape using 16 markers (nascent RNA, RNA-associated proteins, chromatin-associated proteins and histone PTMs, Fig. 2b, Extended Data Fig. 6a) in mouse C127 cells in G1with 40 3D datasets from 2 biological repeats for each marker, each with hundreds to several thousands of annotated IF foci (Extended Data Table 1).

First, we noted that RNA processing/interacting factors hnRNPC1/2, SAF-A (hnRNPU), RNAP-S2P and nascent RNA transcripts are enriched in the IC class 1 and the lowest chromatin classes 2 and 3, while they are depleted in the internalized chromatin classes 4 and 5 and are virtually absent in the highest classes 6 and 7 (Fig. 2b, left). Interestingly, those factors known to interact with chromatin, RNAPII-S2P, nascent RNA and SAF-A, show a peak of enrichment in class 2, while the sole factor that only binds RNA, hnRNPC1/2 shows the strongest enrichment in class 1. Accordingly, average nearest-distance measurements to segmented chromatin boundary result in a mean distance location of hnRNPC1/2 outside of chromatin, while the other three markers centre at the segmented boundary (Fig. 2c, right). These results are in accordance with early immuno-EM observations[37] that active transcription is confined to 'peri-chromatin' at the interface of chromatin domains and the IC. They are also in line with the reported function of SAF-A as an interactor of chromatin-associated RNAs[38] and support the concept of a physical 3D interface between an RNA environment and decondensed outer fringes of chromatin blobs.

Unlike RNA-interacting proteins, the location distribution of segmented histone PTMs, which are inherently chromatin-associated, show a marked depletion in the lowest intensity

class 1, thus validating those annotated voxels as a true interchromatin (IC) compartment. Importantly, we observe a biased enrichment for both H3K4me3, typically located at promoters of active genes, and H3K36me3, typically enriched along the body of transcribed genes (Fig. 2b, left), in the lowest chromatin intensity classes 2 and 3 marking the outer fringe region of the filament, with peak enrichment in class 2 similar to RNAPII-S2P and nascent transcripts. These markers are rarely found in the higher intensity classes 4 and 5, that denote the interior of blobs, and are almost absent in the classes 6 and 7, that mark mainly constitutive heterochromatin (Fig. 2b, left). Their corresponding di-methylated forms (H3K4me2 and H3K36me2), as well as acetylated H4K5, which has been implicated in epigenetic bookmarking[39] also show a notable albeit less distinct enrichment in the lower class range (peak in class 3) and depletion in higher classes.

In contrast, repressive histone PTMs generally show a broader distribution that is shifted towards the higher intensity classes. The H3K27me3 mark, which is typically deposited along Polycomb-mediated silenced genes[40] shows an enrichment in the interior classes (3-5 peaking at class 4). H3K9me3, a marker for transcriptionally inactive facultative and constitutive heterochromatin[40], is found enriched in the interior and heterochromatin classes (3-7) but most abundant in heterochromatin classes (5-7, peak at class 6). H4K20me3, which has been implicated in silencing repetitive DNA (e.g. in chromocenters of mouse cells) and transposons[41] is most strongly enriched in the heterochromatin classes (6 and 7). Again, the di-methylated state H3K9me2 shows a notably less shifted distribution than H3K9me3 peaking at the interior classes (class 4), similar to H3K27me3.

The distribution of CTCF and two sub-units of the cohesin complex Smc3 and Scc1, was characterised by distinct enrichment in surface classes (1-2) and a depletion in the higher classes as well as their distance profile centring at the segmented boundary of the filament (Fig. 2b).

The observed differential enrichment of functional markers can also be considered in light of the specific enzyme complexes responsible for their deposition. Indeed, there is a remarkable inverse correlation, with smaller complex sizes correlating to peak enrichment in higher chromatin classes of the corresponding marker (Fig. 2c), thus supporting the hypothesis that chromatin density acts as a higher-level regulator of genome function by hindering physical accessibility of larger complexes to substrate chromatin[24]. Analysing a subset of markers in human colon (HCT116) and cervical (HeLa) cancer G1 cells, we found highly similar characteristics of differential spatial distributions, confirming the universal nature of the observed zonation (Extended Data Fig. 6b, c). Moreover, we restricted the analysis to volumes of major euchromatic and heterochromatic regions, also denoted as

>10 Mb sized A and B compartments in Hi-C experiments. We sub-divided the nuclear volume into lamina-associated chromatin plus chromocentre regions versus the residual nuclear volume as proxy for B and A compartmentalization, respectively. We find the nanoscale zonation true for both euchromatic A regions as well as heterochromatic B regions (Fig. 2d, Extended Data Fig. 6d), highlighting the fact that both large-scale compartments harbour transcriptionally active and inactive sequences, albeit at different ratios[42] (Extended Data Fig. 6e) deviating from previous models of wholly active 'open' vs inactive 'closed' domains.

In conclusion our high-content 3D super-resolution ChaIN mapping approach highlights a nanoscale zonation of the chromatin filament topology with markers of active transcription and architectural proteins being confined to the surface of the filament blobs and silencing modification being enriched towards the interior, while the IC harbours most RNAs and RNA interacting proteins. The increasing densities of nucleosomes from the surface towards the interior of these blobs may lead to the physical exclusion (or hindrance) of chromatin-associated complexes relative to their size, such that functional zonation is a consequence of accessibility[24].

The local topological landscape is temporarily relaxed during DNA replication and consolidated in replicative senescence

To assess the impact of DNA replication, we identified S-phase cells by short EdU pulse labelling and grouped them into early, mid and late S-phase stages according to characteristic replicon foci distribution pattern[43] before subjecting them to ChaIN analysis. Taking the entire nuclear volume into account, no significant changes of marker distributions could be seen in mouse C127 cells (Extended Data Fig. 7a), with the notable exceptions of Scc1 and H4K20me3 (discussed below). To study whether replication impinges on its direct local environment, we generated an EdU sub-mask of the nucleus that encompasses active replication sites and post-replicative chromatin (Fig. 3a). Overlaying this sub-mask with the segmented chromatin landscape reveals a strong decompaction indicating locally confined disruption, likely caused by activity of the replication machinery. This is most dramatically highlighted by tunnel-like voids becoming apparent in otherwise dense chromocentres in late S-phase (Fig. 3b). Accordingly, EdU labelled replicon foci show an enrichment in the lower chromatin density classes, irrespective of S-phase stage (Fig. 3c).

When quantifying chromatin classes and functional marker distribution in replicating sub-regions, we observed expectedly a shift towards denser chromatin classes when progressing from early, to mid, to late S-phase (Fig. 3d), and a highest abundancy of the

active histone PTM H3K4me3 in early S as compared to the repressive PTM H3K27me3, which was most enriched in mid S phase (Fig. 3e, Extended Data Fig. 7b). Interestingly, the depletion of Scc1 with increasing chromatin density as seen in G1 cells is noticeably mitigated in S phase cells, already for the entire nuclear volume as well as in post-replicative chromatin sub-volumes (Extended Data Fig. 7a, b) indicating an internalisation of cohesin when acting in sister chromatid cohesion. Constitutive heterochromatin mark H4K20me3, on the other hand, becomes less enriched in denser chromatin classes during late S-phase (Extended Data Fig. 7a) with the opening of condensed chromatin. Restricting the analysis to the EdU sub-mask shows a reduced enrichment in higher chromatin classes more so for all repressive histone modifications than for active modifications through S-phase progression (Extended Data Fig. 7b).

Since active replication temporarily opens dense chromatin and relaxes functional marker distribution, we anticipated that replicative senescence (RS) would have the contrary effect. To test this, we applied our Cha*i*N workflow to human IMR-90 cells comparing cycling cells in G1 versus senescent RS cells. Indeed, the chromatin landscape in senescent cells reveals a clear tendency to cluster into senescence-associated heterochromatin foci (SAHFs, Extended Data Fig. 7c). Furthermore, we observed a substantial accentuation of the spatial segregation of active and repressive functional markers in non-cycling cells (Extended Data Fig. 7d).

Our data shows that active DNA replication can locally disrupt both the physical organisation of chromatin and the functional zonation. As replication ceases, a profound stabilisation of functional and structural compartmentalisation may lead to a 'transcriptional lock-in' of gene expression profiles in senescent or terminally differentiated cells.

Biophysical and biochemical perturbations affect 3D chromatin landscape

To better understand the forces and potential mechanisms shaping the observed landscape we next analysed various chemical and biophysical perturbations: (1) transcriptional inhibition using triptolide, a potent inhibitor of RNAPI and RNAPII initiation, (2) reversible induction of hypercondensed chromatin (HCC) by hyperosmolarity-mediated increase of bivalent cations[44], and (3) ATP-depletion through irreversibly blocking of the respiratory chain upon sodium azide (NaN_3) treatment[45]. Chromatin compaction becomes apparent upon ATP depletion and is most prominent in hyperosmolarity induced hypercondensed chromatin with finer filamentous features merging into larger, more compacted features and concurrent widening of the IC (Fig. 4a). Accordingly, when quantifying parameters of the segmented filament we observed an increasing shift of relative voxel number towards higher

intensity classes, while the overall volume ratio between IC class 1 and chromatin classes 2-7 remain constant (Fig. 4c). More strikingly, however, the segmented chromatin surface area to volume ratios (SA:vol) challenged by both hyper-osmotic or triptolide exposure decreases significantly compared to G1 (Fig. 4d) and quantitatively underpin the changes in chromatin observed by 3D-SIM imaging. Concomitantly, we observe a subtle but noticeable increase in volume occupied by the perichromatin classes 2-3 (Fig. 4c), suggesting that transcription initiation acts to constrain the perichromatin volume.

Analysing the spatial distribution of selected markers did not reveal any major change in trend of distribution (Fig. 4b, Extended Data Fig. 8a). We did note an accentuation of elongating RNAPII-S2P, and active transcription histone PTM H3K4me3 accumulating in the surface classes (2-3) as progression from NaN_3 to HCC concomitant with Scc1 and H3K4me3 being even more strongly depleted in the interior and heterochromatin classes (4-7). There is a comparable marked reduction in distribution bias for both repressive histone PTMs (H3K27me3 and H3K9me3) in both NaN_3 and HCC relative to G1, which is also visible in Trip treatment for H3K27me3 but not for H3K9me3. Trip treatment generally lessens depletion for all active markers in the interior and heterochromatin classes (4-7). We see no change in the trend of average marker distances to the segmented chromatin-IC boundary with only Scc1, CTCF and H3K27me3 showing a non-significant move away from the chromatin/IC interface in Trip treatment (and NaN_3 to a lesser magnitude, Extended Data Fig. 8b). Of note, the positioning of RNAPII-S2P remains stable around the segmented chromatin-IC boundary in all analysed perturbations suggesting the underlying biological demarcation of this surface is coupled to elongating transcription. The absolute numbers of detected RNAPII-S2P signals are unchanged in both NaN_3 and HCC relative to G1 (Extended Data Table 1), indicating that elongating RNAPII remains attached to filament surface regions regardless of chromatin being biophysically challenged; the numbers do decrease to one third of those in G1 when transcription initiation is inhibited. For HCC the lack of increased distance to the surface for repressive PTMs when there are increased volumes of denser chromatin shows that repression via histone remodelling is limited to a 40-120 nm depth from the surface. It may be that the hindrance imposed from nucleosome density is sufficient to avoid activation of promoters beyond this depth further supporting *in silico* modelling of nucleosome melts[46].

Together the data shows that overall 3D zonation is unchanged by large-scale rearrangements of the chromatin blob filament through chemical and biophysical forces, even though different perturbations may induce subtle changes for individual markers.

Cohesin function is dispensable for 3D chromatin structure and functional zonation

To test the role of cohesin in maintenance of a TAD-harbouring chromatin filament and the spatial segregation of the 3D epigenome we ablated the SCC1 (RAD21) subunit of the cohesin complex in human HCT116 cells using auxin inducible protease degradation[47] (Extended Data Fig. 9a-c). Upon addition of both doxycycline and auxin, Scc1 can be depleted with a half-life of 17 min[47] to be completely ablated in 2 h (Extended Data Fig. 9d, e). Strikingly, quantitative analysis of HCT116 wild type versus SCC1-mAID cells 6 h after induction does not show any observable change in the chromatin filament structure (Fig. 5a-c) or the absolute deposition of functional histone PTMs on this landscape (Fig. 5d, Extended Data Fig. 9f-h). The chromatin filament diameter and relative chromatin surface area to its volume does not change suggesting that suggesting cohesin is dispensable for these structures.

Cohesin inactivation results in the complete elimination of TADs in Hi-C experiments in HCT116 cells[14]. Our findings therefore demonstrate that loss of cohesin, and thereby TADs, has no observable effect on higher-order structures. We conclude that cohesin and TADs are not vital for maintaining the filament of blobs and are therefore also dispensable for nanoscale functional zonation. We postulate that the role of cohesin is to guide relevant physiological genomic loci to occupy the appropriate zonation generated from the physical properties of chromatinised DNA *in situ*.

Discussion

Our novel high-throughput quantitation reveals that chromatin in somatic interphase cells arranges as a curvilinear filament of sequential discrete chromatin blobs with local viscoelastic dynamic properties and ordered densities that can harbour individual TADs. This filamentous chain-like structure is separated from an RNA-rich interchromatin (IC) network and the transition between these environments encompasses a defined nanoscale zonation of genome functions relative to chromatin density, where active transcription and architectural proteins are confined to the surface area and silencing marks are enriched towards the interior of the nucleosomal entities (Fig. 6a). We show that the principle of 3D zonation is unchanged by large-scale rearrangements of the filament through chemical and biophysical forces, that it correlates with the size of chromatin-associated complexes, but can be locally undermined by active replication or stabilised in non-replicating senescent cells. Importantly, we demonstrate for the first time that nanoscale zonation occurs in both eu- and heterochromatic (A/B) compartments of the nucleus, deviating from previous models of wholly active ‘open’ vs inactive ‘closed’ domains. We postulate that genome segments

with fewer active sites form larger, low-surface, globular blobs (~1 Mb, ~5000 nucleosomes, ~300-500 nm diameter), while segments rich in active sites display an extended, high-surface, topology of smaller volumes (size range ~0.2 Mb, ~1000 nucleosomes, 150-200 nm diameter). In this model the ratio of active surface area to volume is a key determinant of genome activity (Fig. 6b), while providing an explanation of how cell type specific transcriptional programs can be established despite variation in the genomic composition of A/B compartments between cells[48].

Finally, we show cohesin activity to be dispensable for maintaining an interphase filament of consecutive blobs (Fig. 6c, right), in line with a recent study[17]. Given that cohesin is essential for TADs in Hi-C we conclude that chromatin blobs are distinct and not analogous to TADs (Fig. 6c, left). This is consistent with the loop extrusion hypothesis that proposes that TADs emerge in Hi-C experiments due to averaging intermediates of loop extrusion from many cells. The work presented provides a universal structural and dynamic framework of 4D nucleome organisation that guides/modulates the probability of protein (complex)-DNA interactions, thereby changing our perspective of the 3D context in which we frame our knowledge of molecular mechanisms regulating genome function (for further details see Supplementary Discussion).

Acknowledgements

We thank Edith Heard for BACS for providing FISH probes against the Xist TAD. Research in the L.S. laboratory is supported by the Wellcome Trust Strategic Award 107457 funding advanced microscopy at Micron Oxford, and the John Fell Oxford University Press (OUP) Research Fund 143/064. Research visit of H.A.S. in the L.S. lab was enabled by an AfOx travel grant of the Africa-Oxford Initiative. E.M. further acknowledges support by the Sydney Perry Foundation & Covenantors Educational Fund. We thank all colleagues who read and provided comments on the manuscript, in particular Jiri Lukas, Tim Nott and Rob Klose for valuable suggestions.

Author Contributions

E.M. and L.S. conceived the project and designed the experiments. E.M., R.O., H.A.S. and D.M.S.P. wrote the software and performed analyses. J.B. and V.B. devised the FISH protocol. E.M., R.O., J.B., A.R.C.F., S.d.O., C.I., J.R. and L.S. carried out experiments. E.M., R.O. and L.S. wrote the manuscript and generated the figures with contributions from all authors.

REFERENCES

1. Gibcus, J. H. & Dekker, J. The Hierarchy of the 3D Genome. *Mol. Cell* **49,** 773–782 (2013).
2. Pombo, A. & Dillon, N. Three-dimensional genome architecture: players and mechanisms. *Nat. Rev. Mol. Cell Biol.* **16,** 245–257 (2015).
3. Luger, K., Mäder, A. W., Richmond, R. K., Sargent, D. F. & Richmond, T. J. Crystal structure of the nucleosome core particle at 2.8 A resolution. *Nature* **389,** 251–60 (1997).
4. Cremer, T. & Cremer, C. Chromosome territories, nuclear architecture and gene regulation in mammalian cells. *Nat. Rev. Genet.* **2,** 292–301 (2001).
5. Adriaens, C. *et al.* Blank spots on the map: some current questions on nuclear organization and genome architecture. *Histochem. Cell Biol.* **150,** 579–592 (2018).
6. Lieberman-Aiden, E. *et al.* Comprehensive Mapping of Long-Range Interactions Reveals Folding Principles of the Human Genome. *Science.* **326,** 289–293 (2009).
7. Dixon, J. R. *et al.* Topological domains in mammalian genomes identified by analysis of chromatin interactions. *Nature* **485,** 376–380 (2012).
8. Lupiáñez, D. G. *et al.* Disruptions of topological chromatin domains cause pathogenic rewiring of gene-enhancer interactions. *Cell* **161,** 1012–1025 (2015).
9. Phillips, J. E. & Corces, V. G. CTCF: Master Weaver of the Genome. *Cell* **137,** 1194–1211 (2009).
10. Parelho, V. *et al.* Cohesins Functionally Associate with CTCF on Mammalian Chromosome Arms. *Cell* **132,** 422–433 (2008).
11. Alipour, E. & Marko, J. F. Self-organization of domain structures by DNA-loop-extruding enzymes. *Nucleic Acids Res.* **40,** 11202–11212 (2012).
12. Fudenberg, G. *et al.* Formation of Chromosomal Domains by Loop Extrusion. *Cell Rep.* **15,** 2038–2049 (2016).
13. Ganji, M. *et al.* Supplementary materials for Real-time imaging of DNA loop extrusion by condensin. *Science.* **360,** 102–105 (2018).
14. Rao, S. S. P. *et al.* Cohesin Loss Eliminates All Loop Domains. *Cell* **171,** 305–320.e24 (2017).
15. Nagano, T. *et al.* Single-cell Hi-C reveals cell-to-cell variability in chromosome structure. *Nature* **502,** 59–64 (2013).
16. Flyamer, I. M. *et al.* Single-nucleus Hi-C reveals unique chromatin reorganization at oocyte-to-zygote transition. *Nature* **544,** 110–114 (2017).
17. Bintu, B. *et al.* Super-resolution chromatin tracing reveals domains and cooperative interactions in single cells. *Science.* **362,** eaau1783 (2018).
18. Finn, E. H. *et al.* Heterogeneity and Intrinsic Variation in Spatial Genome Organization. *Cell* (2019). doi:10.1016/j.cell.2019.01.020
19. Nora, E. P. *et al.* Spatial partitioning of the regulatory landscape of the X-inactivation centre. *Nature* **485,** 381–385 (2012).
20. Fabre, P. J. *et al.* Nanoscale spatial organization of the *HoxD* gene cluster in distinct

transcriptional states. *Proc. Natl. Acad. Sci.* **112,** 13964–13969 (2015).

21. Szabo, Q. *et al.* TADs are 3D structural units of higher-order chromosome organization in Drosophila. *Sci. Adv.* **4,** 1–14 (2018).
22. Maeshima, K. *et al.* Nucleosomal arrays self-assemble into supramolecular globular structures lacking 30-nm fibers. *EMBO J.* **35,** 1115–1132 (2016).
23. Boettiger, A. N. *et al.* Super-resolution imaging reveals distinct chromatin folding for different epigenetic states. *Nature* **529,** 418–422 (2016).
24. Maeshima, K. *et al.* The physical size of transcription factors is key to transcriptional regulation in chromatin domains. *J. Phys. Condens. Matter* **27,** 064116 (2015).
25. Schermelleh, L. *et al.* Super-resolution microscopy demystified. *Nat. Cell Biol.* **21,** 72–84 (2019).
26. Schermelleh, L. *et al.* Subdiffraction Multicolor Imaging of the Nuclear Periphery with 3D Structured Illumination Microscopy. *Science.* **320,** 1332–1336 (2008).
27. Markaki, Y. *et al.* Functional nuclear organization of transcription and DNA replication: A topographical marriage between chromatin domains and the interchromatin compartment. *Cold Spring Harb. Symp. Quant. Biol.* **75,** 475–492 (2010).
28. Smeets, D. *et al.* Three-dimensional super-resolution microscopy of the inactive X chromosome territory reveals a collapse of its active nuclear compartment harboring distinct Xist RNA foci. *Epigenetics Chromatin* **7,** 8 (2014).
29. Kanda, T., Sullivan, K. F. & Wahl, G. M. Histone–GFP fusion protein enables sensitive analysis of chromosome dynamics in living mammalian cells. *Curr. Biol.* **8,** 377–385 (1998).
30. Jao, C. Y. & Salic, A. Exploring RNA transcription and turnover in vivo by using click chemistry. *Proc. Natl. Acad. Sci.* **105,** 15779–15784 (2008).
31. Shaban, H. A., Barth, R. & Bystricky, K. Formation of correlated chromatin domains at nanoscale dynamic resolution during transcription. *Nucleic Acids Res.* **46,** e77 (2018).
32. Bruinsma, R., Grosberg, A. Y., Rabin, Y. & Zidovska, A. Chromatin hydrodynamics. *Biophys. J.* **106,** 1871-1881 (2014).
33. Markaki, Y. *et al.* The potential of 3D-FISH and super-resolution structured illumination microscopy for studies of 3D nuclear architecture. *BioEssays* **34,** 412–426 (2012).
34. Brown, J. M. *et al.* A tissue-specific self-interacting chromatin domain forms independently of enhancer-promoter interactions. *Nat. Commun.* **9,** 1–15 (2018).
35. Zuin, J. *et al.* Cohesin and CTCF differentially affect chromatin architecture and gene expression in human cells. *Proc. Natl. Acad. Sci.* **111,** 996–1001 (2014).
36. Kraus, F. *et al.* Quantitative 3D structured illumination microscopy of nuclear structures. *Nat. Protoc.* **12,** 1011-1028 (2017).
37. Fakan, S. & van Driel, R. The perichromatin region: A functional compartment in the nucleus that determines large-scale chromatin folding. *Semin. Cell Dev. Biol.* **18,** 676–681 (2007).
38. Nozawa, R. S. *et al.* SAF-A Regulates Interphase Chromosome Structure through Oligomerization with Chromatin-Associated RNAs. *Cell* **169,** 1214–1227.e18 (2017).

39. Zhao, R., Nakamura, T., Fu, Y., Lazar, Z. & Spector, D. L. Gene bookmarking accelerates the kinetics of post-mitotic transcriptional re-activation. *Nat. Cell Biol.* **13,** 1295–1304 (2011).
40. Dambacher, S., Hahn, M. & Schotta, G. Epigenetic regulation of development by histone lysine methylation. *Heredity (Edinb).* **105,** 24–37 (2010).
41. Schotta, G. *et al.* A silencing pathway to induce H3-K9 and H4-K20 trimethylation at constitutive heterochromatin. *Genes Dev.* **18,** 1251-1262 (2004).
42. Rowley, M. J. & Corces, V. G. Organizational principles of 3D genome architecture. *Nat. Rev. Genet.* **13,** (2018).
43. Chagin, V. O. *et al.* 4D Visualization of replication foci in mammalian cells corresponding to individual replicons. *Nat. Commun.* **7,** 11231 (2016).
44. Albiez, H. *et al.* Chromatin domains and the interchromatin compartment form structurally defined and functionally interacting nuclear networks. *Chromosom. Res.* **14,** 707–733 (2006).
45. Gorisch, S. M. *et al.* Nuclear body movement is determined by chromatin accessibility and dynamics. *Proc. Natl. Acad. Sci.* **101,** 13221-13226 (2004).
46. Maeshima, K., Hihara, S. & Eltsov, M. Chromatin structure: Does the 30-nm fibre exist in vivo? *Curr. Opin. Cell Biol.* **22,** 291–297 (2010).
47. Natsume, T., Kiyomitsu, T., Saga, Y. & Kanemaki, M. T. Rapid Protein Depletion in Human Cells by Auxin-Inducible Degron Tagging with Short Homology Donors. *Cell Rep.* **15**, 210-218 (2016).
48. Joffe, B., Leonhardt, H. & Solovei, I. Differentiation and large scale spatial organization of the genome. *Curr. Opin. Genet. Dev.* **20,** 562–569 (2010).

FIGURES

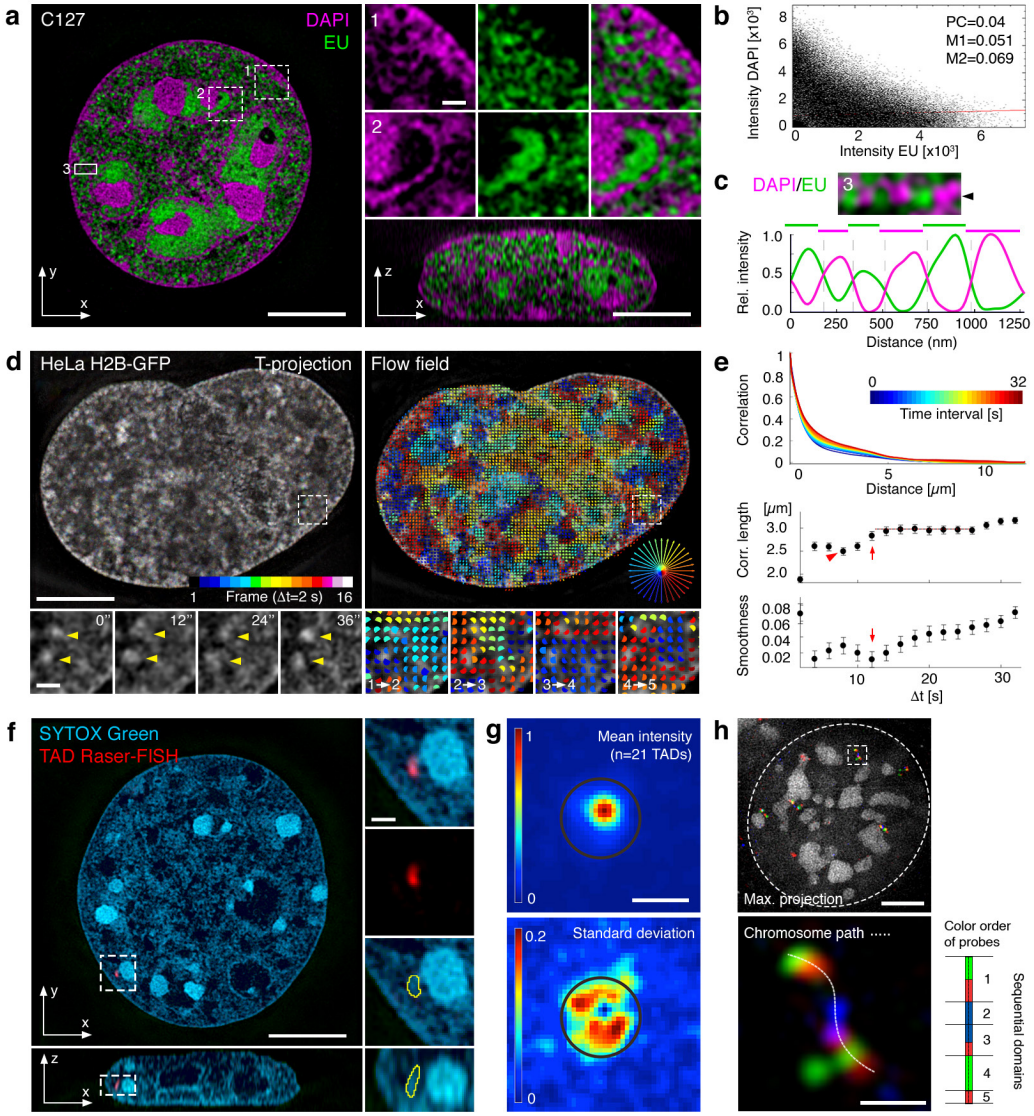

Figure 1 | Chromatin folds into a 3D filament of 'blobs' distinct from an RNA-occupied interchromatin network. a, Super-resolution 3D-SIM of fixed mouse C127 mammary epithelial cells resolves DAPI-stained chromatin as a porous convoluted filament juxtaposed to a volume of non-chromatin (interchromatin, IC) channels where RNA resides (EU, 60 min pulse). Right, inset magnifications of regions 1 and 2, and orthogonal cross section. **b**, Pixel-based colocalisation analysis scatter plot confirms anti-correlation of DAPI and EU signal. PC: Pearson correlation coefficient; M1/M2: Manders' correlation coefficients DAPI vs. EU and EU vs. DAPI, respectively. **c**, Line profile of signal intensity for both DAPI and EU from a representative euchromatic region in panel (a) reveal mutually exclusive volumes occupied by both nucleic acids. **d,** Live cell 3D-SIM of a human HeLa cell stably expressing histone H2B-GFP. Left panel: Colour-coded projection of 16 consecutive time-points recorded with 2 s intervals (Supplementary Movie 1). Inset magnifications of selected individual time-points showing coherently moving domains (arrow heads). Right panel: Overlay of flow field indicating motion direction. Fields are colour-coded according to the direction of the displacement (Supplementary Movie 4). Insets show analyses for the first 4 intervals with a

time lag of 1 frame (Δ=2 s). **e**, Correlation function is calculated as a function of distance at every accessible time interval (Δt colour coded from short to high time intervals, from blue to red, respectively) within the image series and each of them was fitted to the Whittle–Matérn model. **f**, Correlation length and smoothness parameter are calculated over time for directional correlation of flow fields. Further quantitative analysis of motion fields was performed to extract biophysical parameters and types of motions to characterize diffusion processes at different scales (Methods; Extended Data Fig. 2b). **d**, RASER-FISH detection of a 0.7 Mb labelled TAD (red) and SYTOX Green whole chromatin labelling (cyan) in a mouse C127 cell imaged by 3D-SIM. **e**, Quantification of the mean intensity of 21 TADs. For each TAD, the z-plane containing the brightest pixel was selected, centred with respect to this pixel and normalized to its signal intensity (top). The standard deviation (SD, bottom) describes the degree of variation in TAD size, indicated with a diameter of ~500 nm. **f**, Multicolour FISH labelling of sequential domains across the α-globin gene locus detected in mouse C127 cells. Maximum projections of 3D-SIM micrographs show the genomic order of the probes is preserved as a curvilinear filament of discrete chromatin blobs in space. Scale bars: 5 μm and 0.5 μm (insets).

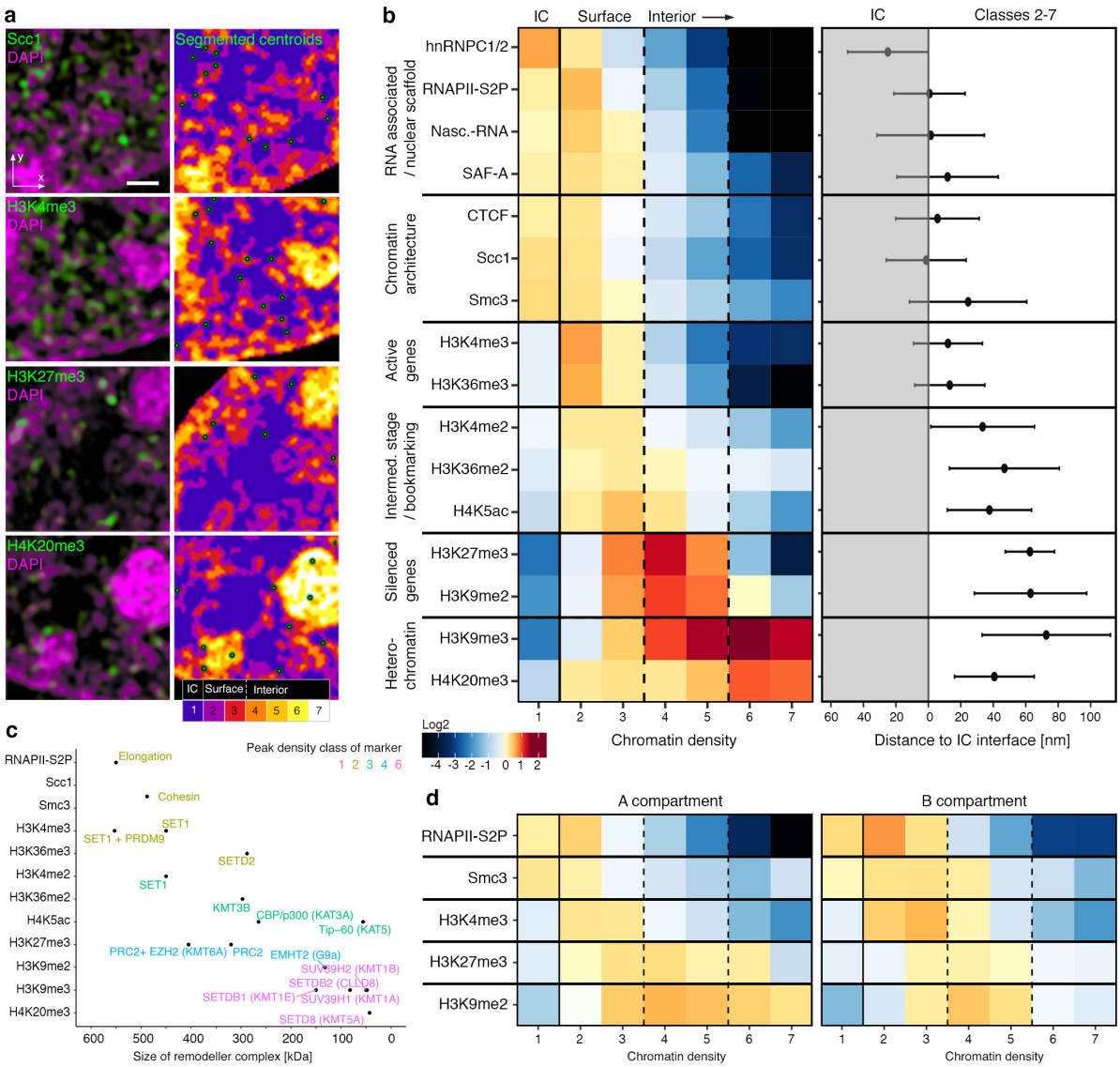

Figure 2 | Functional marker distribution in somatic cells reveals nanoscale 3D zonation correlated with protein complex size. a, Representative single Z planes of 3D-SIM image stacks comparing the spatial localization of different markers with respect to chromatin. Marker centroid coordinates are depicted as green dots with a black outline for regions where the centroid is in the z plane shown. Scale bar: 0.5 μm. **b**, Left: Heatmap of enrichment or depletion of IF signals relative to a random distribution (plotted in log2-fold change) per chromatin density class for all markers. Right: Distance to the chromatin-IC boundary for all markers. Distances on the left (grey) emanate from the IC and on the right (white) emanate from chromatin. The mean distance and 95% confidence interval of the population are shown. N = 433 cells. **c**, Scatterplot showing the correlation between the size of the chromatin complexes corresponding to each of the analysed markers and the peak chromatin class where each marker is found. MW for cohesin was calculated from Smc1, Smc3, Scc1 and Scc3. **d**, Heatmaps relative IF signals distribution of representative markers in nuclear sub-volumes harbouring mainly heterochromatin characteristic for B compartments (segmented perinuclear rim and chromocenter regions), or euchromatin characteristic for A compartments (remaining volume). Both compartments show a relatively

conserved zonation pattern despite the different composition of chromatin density in either A or B regions (Extended Data Fig. 5d). N = 170 cells.

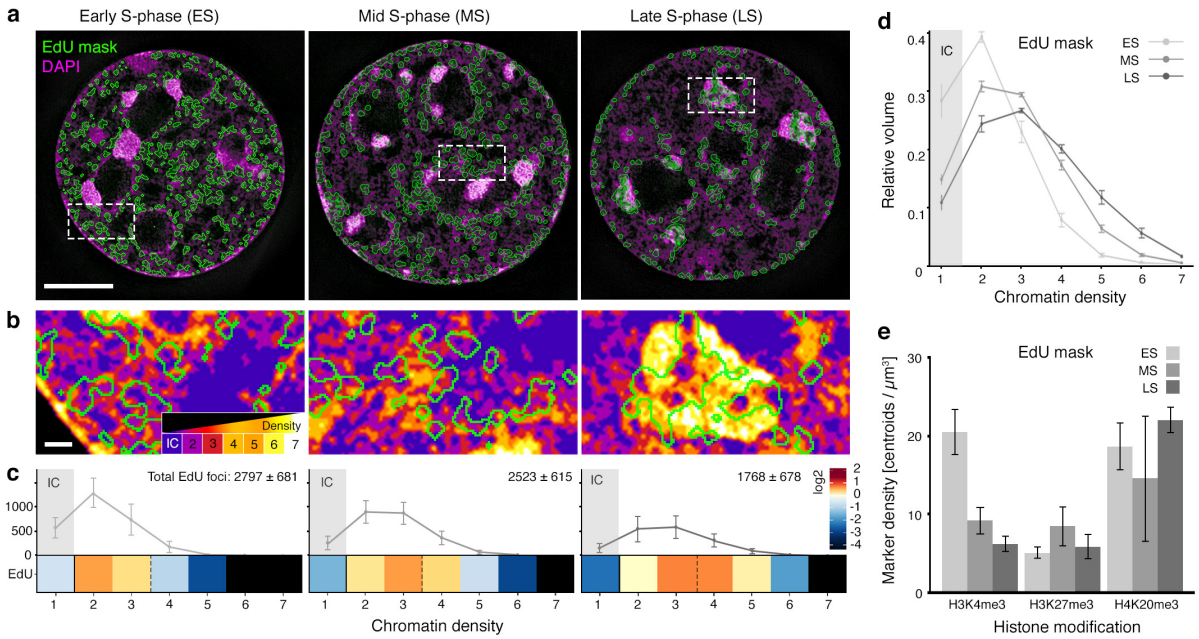

Figure 3 | Effect of active replication and replicative senescence on chromatin composition. a, Representative single Z planes of 3D-SIM images showing the chromatin landscape with the different patterns of replication (green) during S-phase progression from early, mid and late S-phase stages (left to right). Chromatin is stained with DAPI and replication is stained using 15 minutes of EdU incorporation. Local replication regions were masked based on the EdU signal and outlined in green. Scale bar: 5 μm. **b**, Insets of respective boxes indicated in A in which the EdU submask (green outline) is overlaid on the segmented chromatin landscape. Scale bar: 0.5 μm. **c**, Quantification of the absolute number of detected EdU foci in each of the different chromatin classes. The total number of EdU foci per cell is indicated as mean ± SD. Per S-phase stage, a heatmap of enrichment or depletion of EdU signals relative to a random distribution (plotted in log2-fold change) is depicted. **d**, Percentage of chromatin volume of the different density classes to EdU submask volume per S-phase stage. The mean percentage ± SD are depicted. **e**, Foci number per cubic μm EdU submask volume for the depicted histone PTMs in each condition (Extended Data Fig. 7) per S-phase stage. Mean ± SD are depicted. Number of cells: ES = 225, MS =227, LS =230.

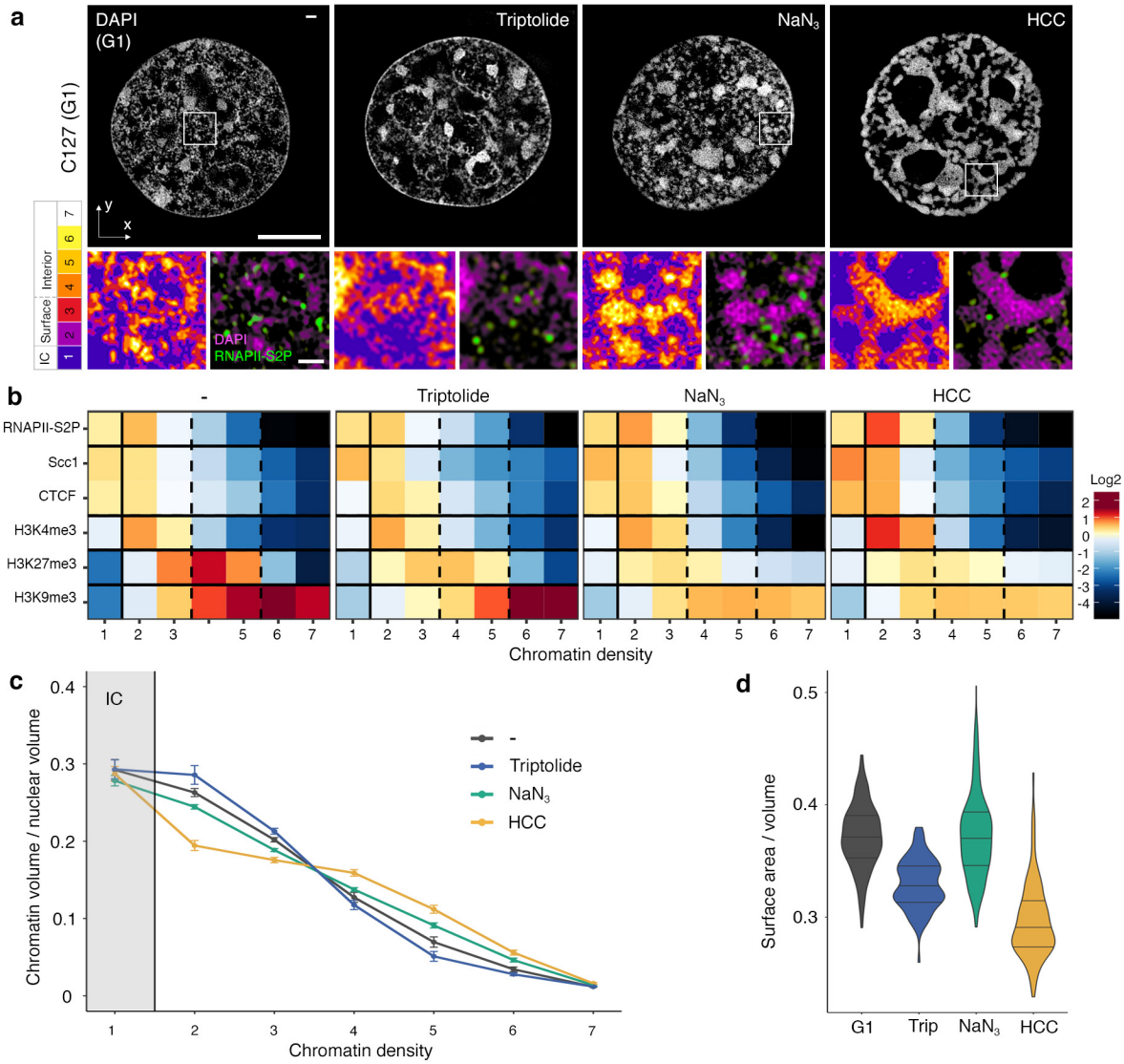

Figure 4 | Epigenome zonation persists after induced perturbation of filament topology. a, Gallery depicting the progressive spatial rearrangement of the filament by the effects of triptolide, sodium azide (NaN_3), hyperosmolarity-induced chromatin compaction (HCC), compared to untreated C127 G1 cells (-). Left insets show density class distribution, right inset shows position of RNAP-S2P at the filament's 3D boundary. **b**, Heatmap of enrichment or depletion of IF signals from a representative subset of markers comparing untreated vs. NaN_3, hyperosmolarity and triptolide treated cells. **c**, Proportion of nuclear volume for each chromatin density class. None of the treatments perturb the IC volume (± 95%CI), but for NaN_3 and HCC there is loss of low-density chromatin (class 2-3) and increase in higher density chromatin (classes 4-7), while triptolide has the opposite effect. **d** Violin plot of surface area to volume ratio of the filament in untreated (-) G1 cells or after treatment with triptolide (Trip), NaN_3or HCC, showing a decrease in filament complexity, quartiles marked. Number of cells: G1 = 210, NaN_3 = 120, HCC =120, Trip=123. Scale bars: 5 μm and 0.5 μm (insets).

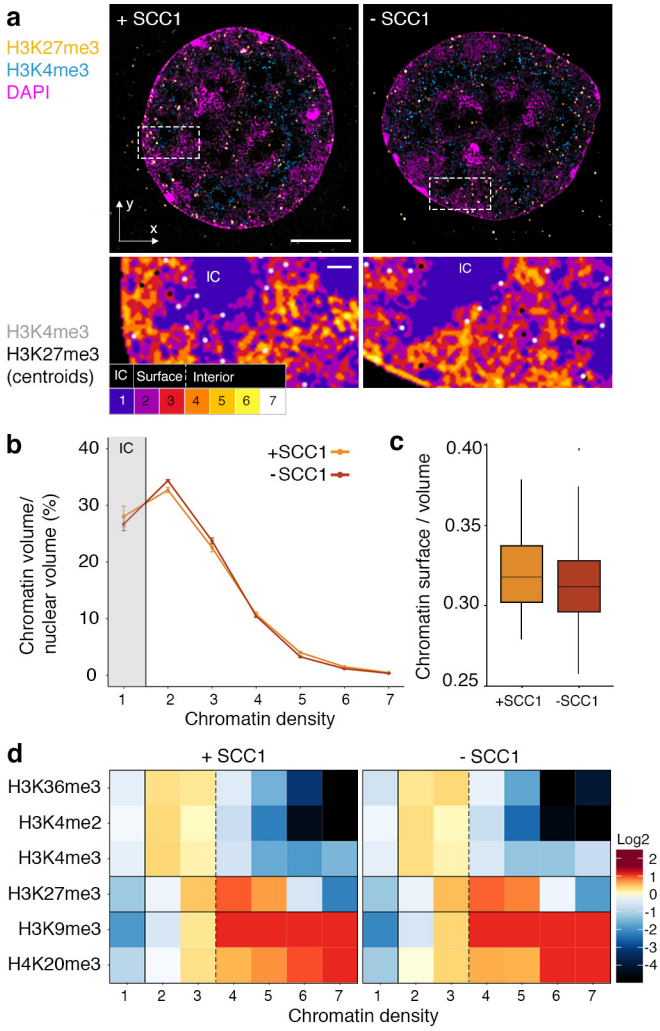

Figure 5 | Cohesin ablation does not affect epigenome topology. a, Representative single z-planes of 3D-SIM images comparing the chromatin landscape in HCT116 cells control cells only treated with auxin for 6 h (+SCC1, left) or SCC1 ablated cells after 16 h doxycycline and 6 h auxin treatment (-SCC1, right). Insets show the segmented landscape with the spatial distribution of H3K4me3 and H3K27me3 represented as green and red dots respectively. **b**, Proportion of nuclear volume for each chromatin density class show no significant change under ablation of cohesin function (± 95%CI). **c**, Heatmap of enrichment or depletion of IF signals from a representative subset of histone modifications. Number of cells: +SCC1 = 80; -SCC1 = 104. Scale bars: 5 μm and 0.5 μm (insets).

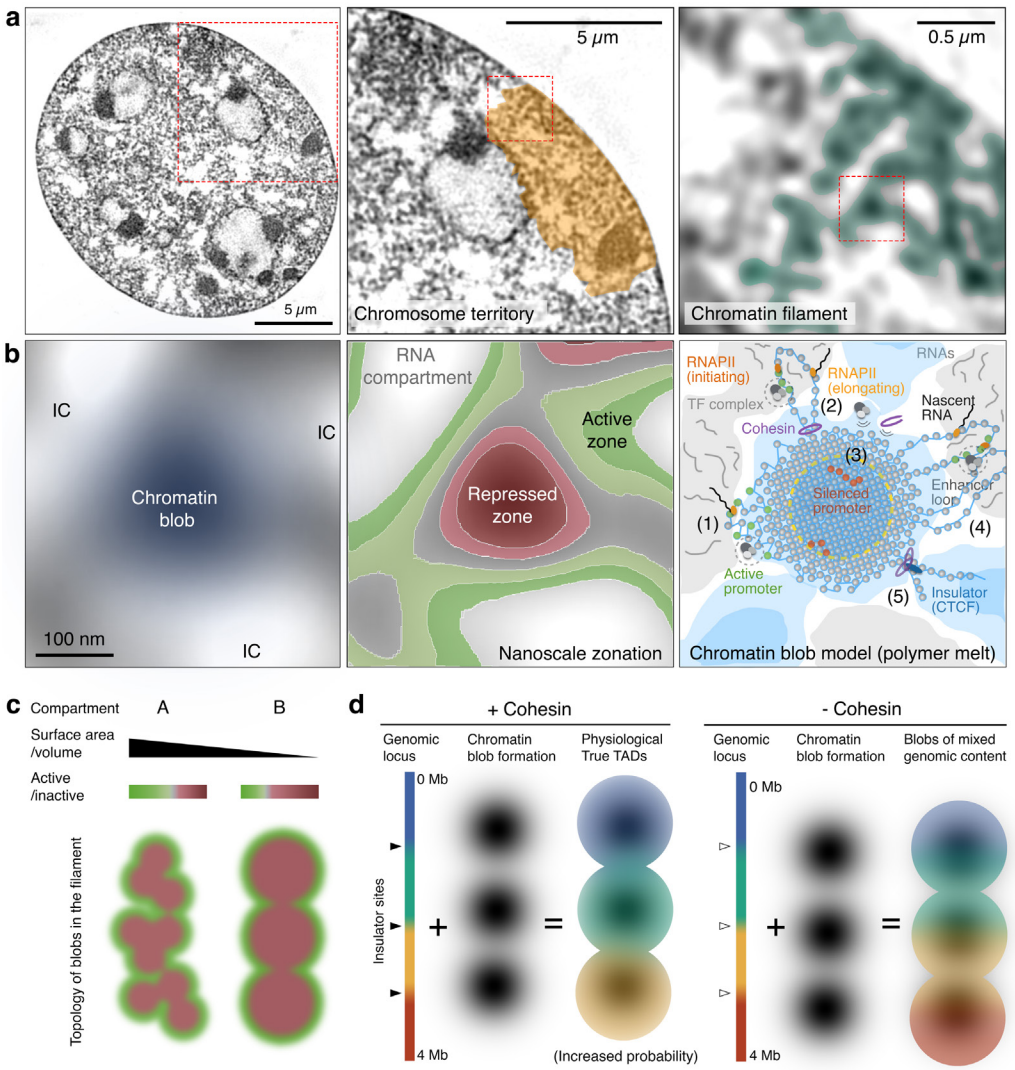

Figure 6 | Model of the chromatin as a filament of blobs. a. Serial magnifications of super-resolved interphase chromatin stained with DAPI in C127 with an overlaid representation of a putative chromosome territory (centre). Chromatin can be described as a curvilinear filament of chromatin blobs. **b**, Zoom-in to an individual blob (left) where zonation at the nm scale is a function of density (centre) modelled by the radial position of histones with diverse PTMs and protein complexes (right). Beyond ~100nm from the blob surface to the IC almost no markers are detected such that any silenced promoter at this "depth" (yellow dashed circle) may remain inactive by being inaccessible to the replication machinery rather than through competition by deposition of repressive histone PTMs. **c**, The ratio of active surface area to volume is a key determinant of genome activity. Changes in TAD topology in either A or B compartments lead to changes in this ratio and give rise to a generally active vs inactive compartment. **d**, Folding of the genome into biophysically defined blobs in the absence of cohesin leads to blob structures without physiologically relevance (multiple colours mixed over genomic insulator boundaries, right). Addition of cohesin, while dispensable for globule formation, links the 3D structure to the correct 1D genomic context leading to physiologically relevant interactions observed as "true TADs" in population Hi-C (left)**.**

EXTENDED DATA FIGURES

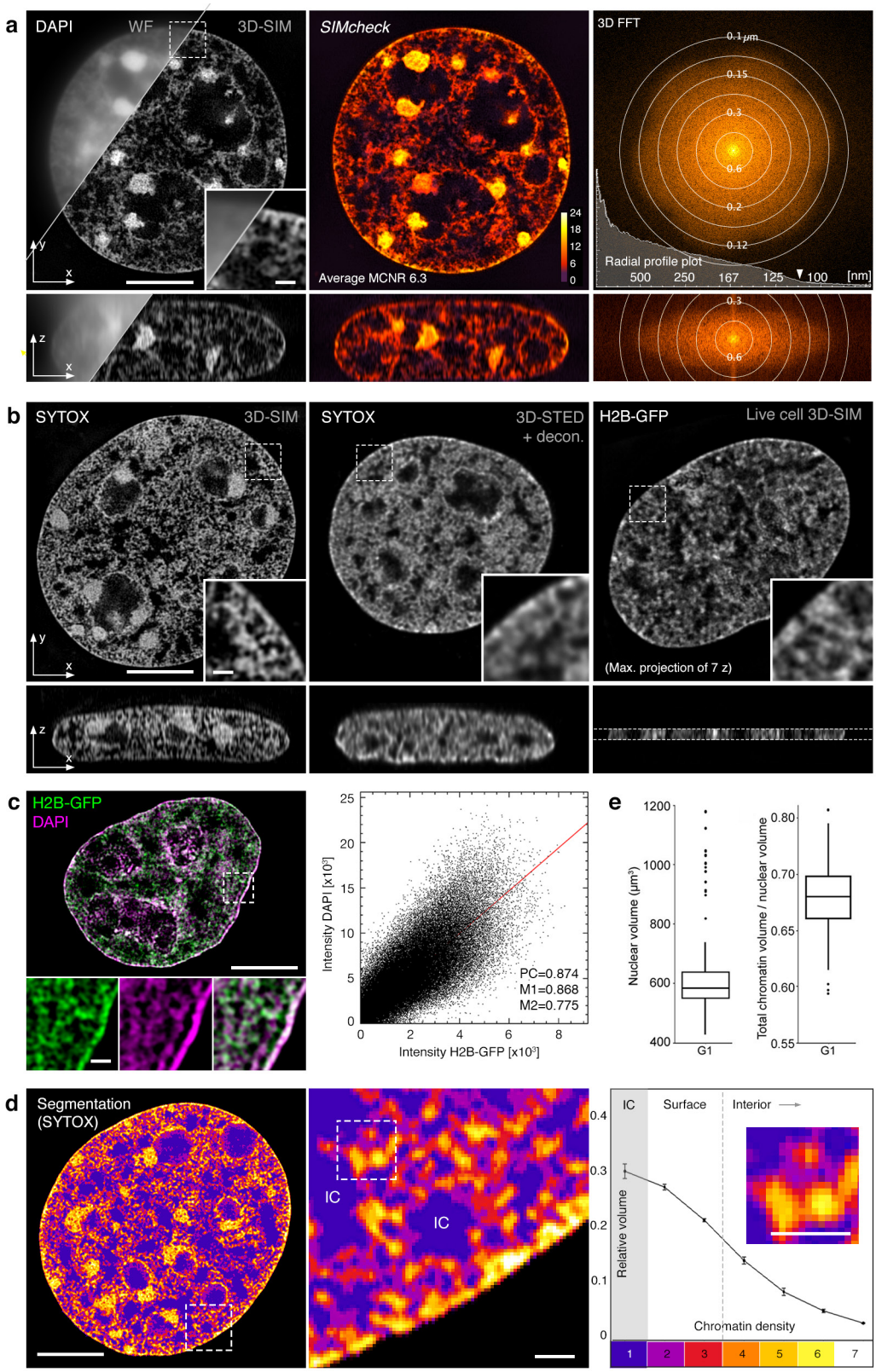

Extended Data Figure 1 | Super-resolution imaging of chromatin. a, 3D-SIM data quality control. Left panel: Comparison of widefield (WF) and corresponding 3D-SIM image of a mouse C127 cell nucleus stained with DAPI (excited with 405 nm, detected in green

emission of 500-550 nm); lateral (top) and orthogonal (bottom) cross section is displayed. Middle and right panel: corresponding quality control analysis using SIMcheck[53], showing a mapping of local stripe modulation contrast (MCNR, modulation contrast to noise ratio) on the reconstructed cross section (middle), and the corresponding axial and lateral Fourier plot with corresponding spatial resolution indicated by concentric rings (right). Superimposed radial profile plot indicates an effective lateral resolution of ~110 nm (arrow head). **b**, Comparison of 3D-SIM (left) and 3D STED (middle) of formaldehyde fixed cells stained with DAPI or SYTOX green staining in C127 cells, as well as live cell 3D-SIM of histone H2B-GFP in a human RPE-1 cell (right, projection of 7 z-planes covering 0.75 μm depth). In all cases, 3D super-resolution imaging allows to resolve filamentous chromatin organisation with globular features and IC network. **c**, DAPI-stained fixed H2B-GFP 3D-SIM and corresponding colocalisation analysis shows strong correlation of both signals. PC: Pearson correlation coefficient; M1/M2: Manders' correlation coefficients DAPI vs. H2B-GFP and H2B-GFP vs. DAPI, respectively. **d**, Segmentation of chromatin staining into 7 intensity (density) classes (Methods) distinguishes interchromatin (IC, class 1) from chromatin of increasing density (classes 2-7). Chromatin density classification serves as a proxy for surface and interior regions of filamentous chromatin. Right: Quantification of class sizes show a decrease of nuclear volume fractions as density increases. **e**, Quantification of nuclear volumes in C127 G1 cells from all segmented voxels shows a mean of ~600 μm^3, of which 68% is occupied by segmented chromatin (classes 2-7). Scale bars: 5 μm and 0.5 μm (insets).

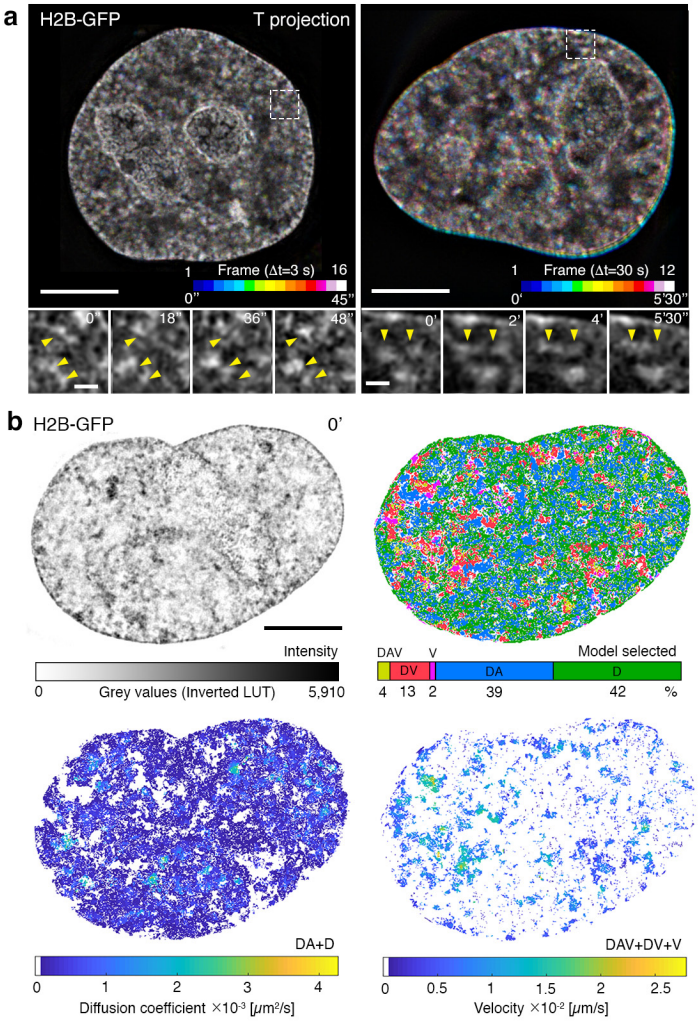

Extended Data Figure 2 | Analysis of chromatin dynamics in from live cell 3D-SIM. a, Live cell 3D-SIM of human HeLa cells stably expressing histone H2B-GFP recorded with intervals of 3 s (left, Supplementary Movie 2) and 30 s (right, Supplementary Movie 3). Colour-coded projection of 16 consecutive time-points. Inset magnifications show selected time-points of the boxed region as maximum projection of 7 z-sections (0.75 μm depth). **b**, Quantitative analysis of motion fields is applied using Bayesian model selection to define types of diffusion processes acting on the chromatin fibre at the local and global scale[49]. The mapping highlights the dynamic heterogeneity of chromatin motion. The spatial distribution of the selected models for each pixel is shown as a colour map, where D: Free diffusion; DA: Anomalous diffusion; V: Drift velocity of flow fields; DV: Free diffusion + drift; DAV Anomalous diffusion + drift. Scale bars: 5 μm and 0.5 μm (insets).

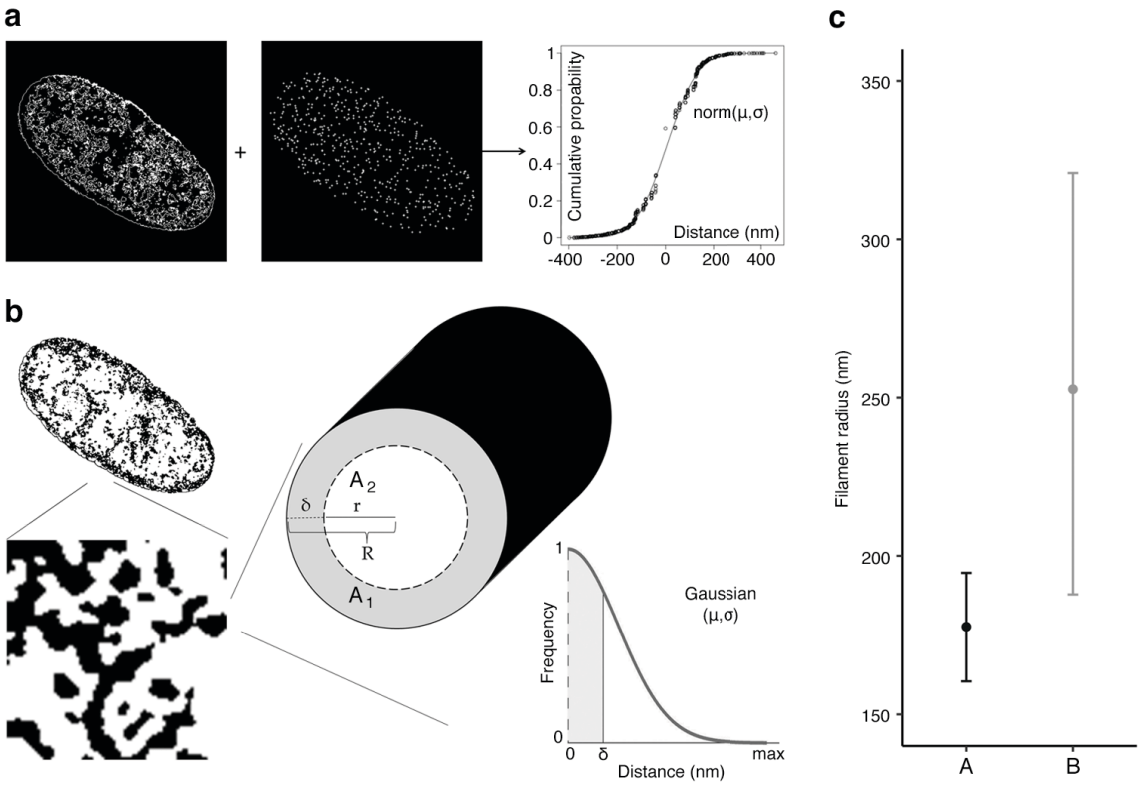

Extended Data Figure 3 | Calculation of filament dimensions. a, A random scatter of 3D points in silico (restrained to the volume of the nucleus, centre) can be used to calculate a random sampling of distances to the boundary (left) between the IC and filament signal. A least square fitting to the cumulative probability of the whole distribution yields mean distance (μ) and standard deviation (σ). **b**, From empirical observation the filament can be approximated as a sponge-like structure of tubular filaments with a degree of variability in width but with an average radius of R. From this model, by simple calculus, the average radius of the filament can be calculated (Methods). **c**, Separating the nuclear volume into macro-scale A and B compartments defined by the lack or presence of lamina-association and chromocenter-morphology yields a filament radius of 175nm for the more tubular like A compartment (diameter 350nm). The B compartment is larger, however, being less tube-like there is decrease accuracy in radial estimation (error bars 95% confidence).

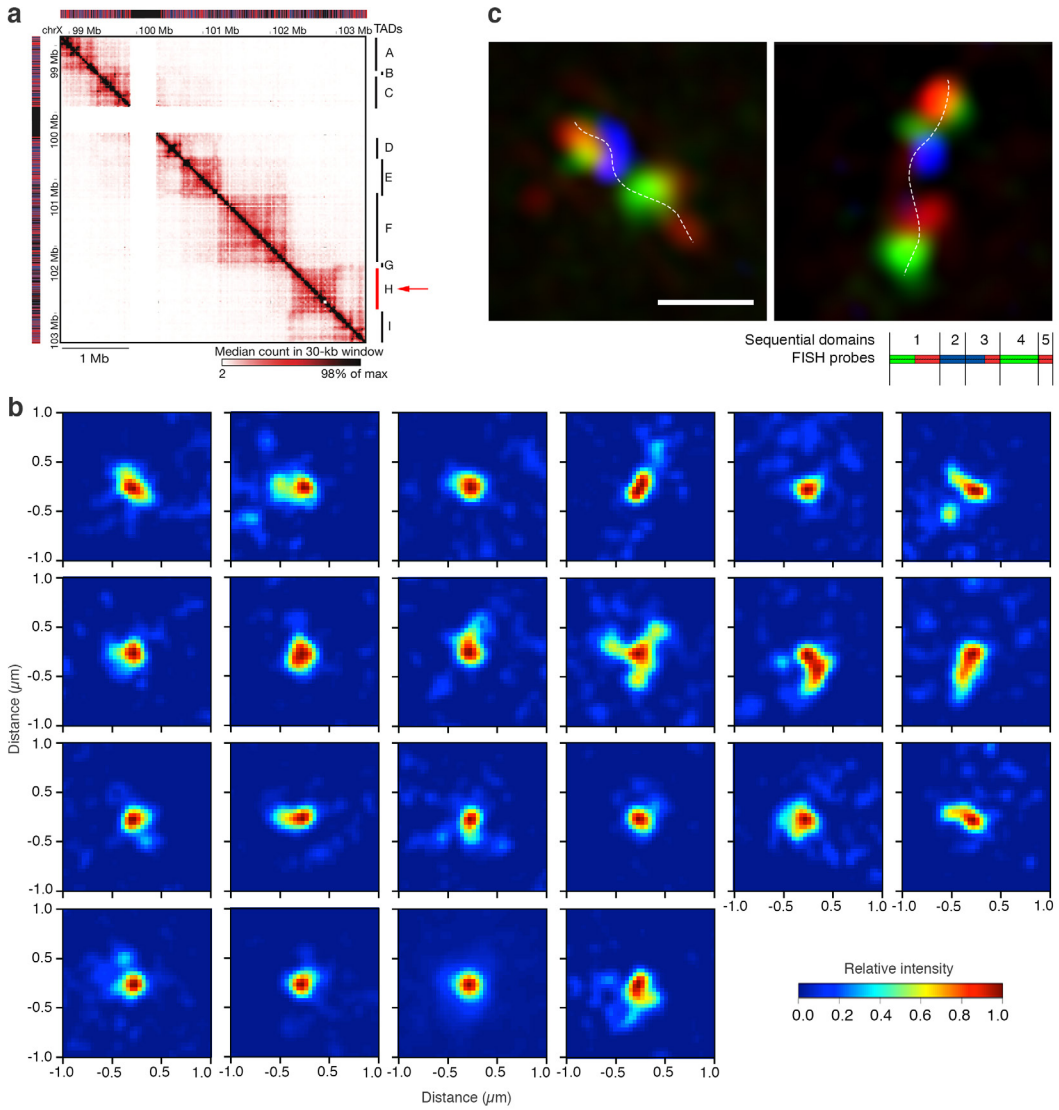

Extended Data Figure 4 | RASER-FISH for imaging chromatin conformation. a, Hi-C heatmap showing the interaction frequency in the 700kb probe (probe H, red bar) used in this study for subsequent RASER-FISH experiments (adapted from[19]). **b**, Super-resolved heatmaps of single Z planes of H TADs on the active X chromosome. TADs were selected based on the absence of the inactive Barr body and for the displayed z planes to contain the brightest pixel of the TAD z-stack. Signal intensity was normalized to the brightest pixel. **c**, Max projections 3D-SIM micrographs of multicolour FISH labelling of sequential domains across the α globin locus. The linear genomic order of the probes (green, red, blue, red, green, red) is preserved as a curvilinear path in 3D (dotted line). Scale bar: 0.5 μm.

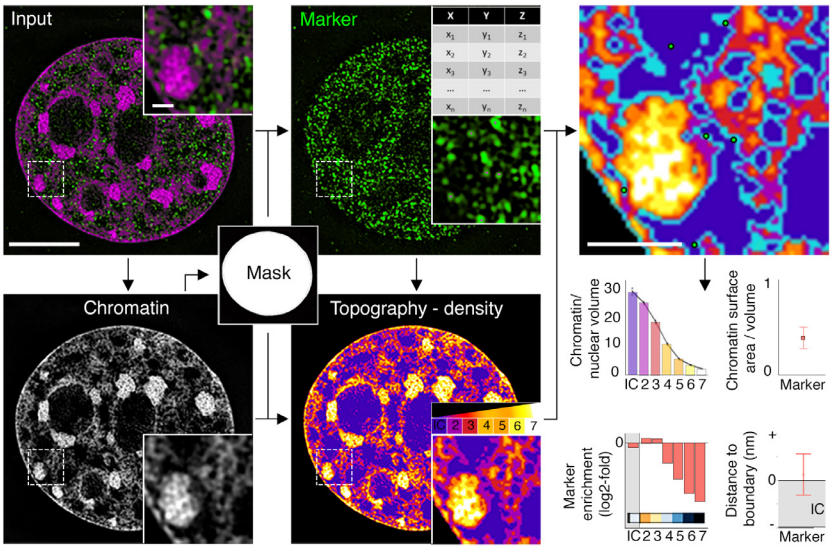

Extended Data Figure 5 | Systematic analysis of the 3D epigenome. Schematic representation of the Cha*i*N analysis workflow. Inputs for the workflow are multi-channel 3D-SIM datasets that have been pre-processed, thresholded and aligned. Firstly, a nucleus mask is generated based on the chromatin channel. Secondly, within this mask, marker spots are segmented by intensity and their weighted centroid positions are determined. Simultaneously, the chromatin channel is segmented in 7 intensity "classes", reflecting increasing chromatin compaction. Finally, metrics from both marker and chromatin channel are used to describe the 3D epigenome, such as the nuclear proportion of each chromatin class, the chromatin surface-to-volume ratio, the marker enrichment or depletion in each chromatin class or the mean distance (± 95% CI) of markers to the segmented chromatin-interchromatin boundary. Analysis was performed using scripts written in R and Octave. Scale bars: 5 μm and 0.5 μm (insets).

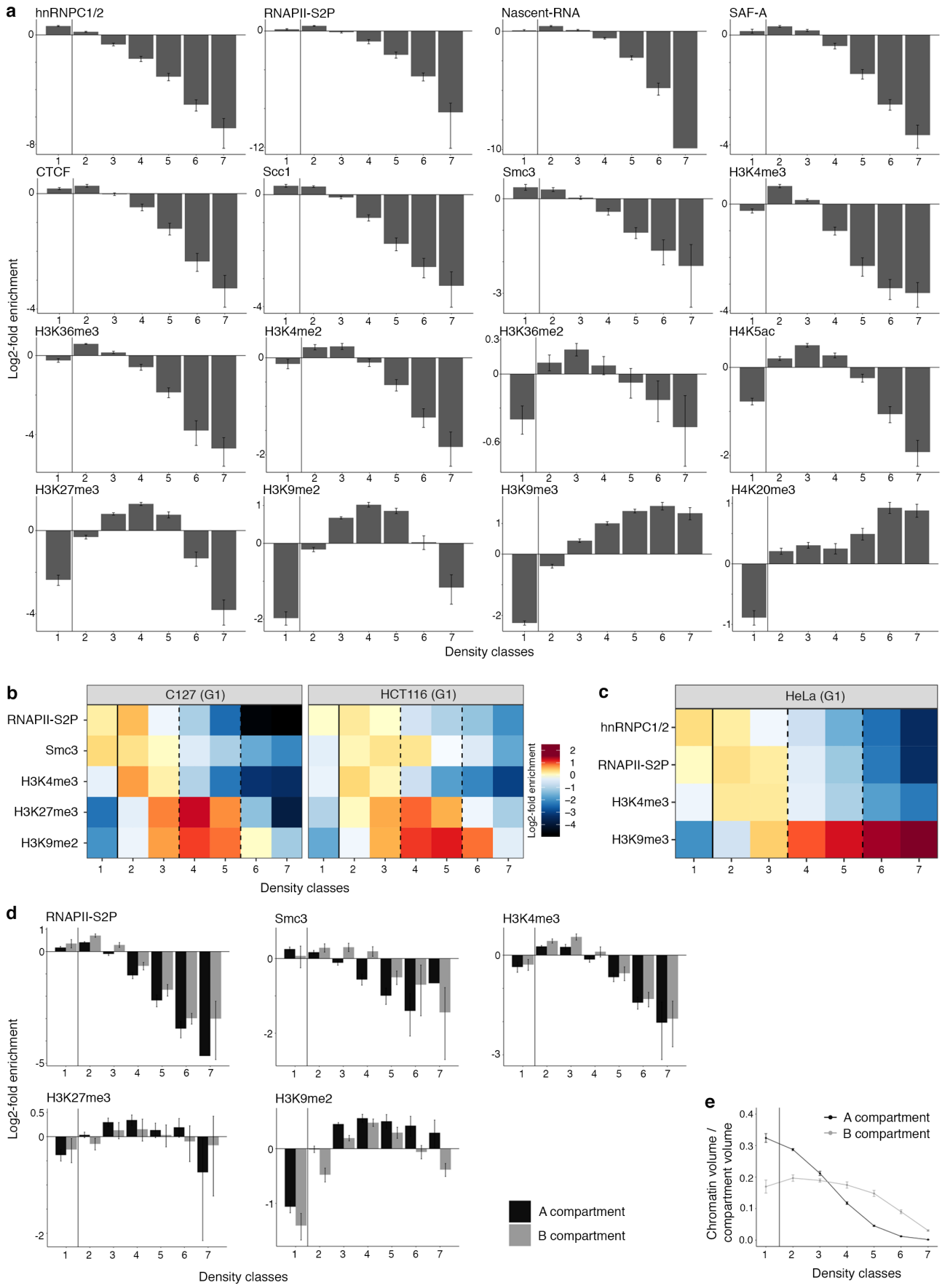
a
hnRNPC1/2
RNAPII-S2P
Nascent-RNA
SAF-A
CTCF
Scc1
Smc3
H3K4me3
H3K36me3
H3K4me2
H3K36me2
H4K5ac
H3K27me3
H3K9me2
H3K9me3
H4K20me3
Log2-fold enrichment
Density classes
b
C127 (G1)
HCT116 (G1)
RNAPII-S2P
Smc3
H3K4me3
H3K27me3
H3K9me2
Log2-fold enrichment
Density classes
c
HeLa (G1)
hnRNPC1/2
RNAPII-S2P
H3K4me3
H3K9me3
d
RNAPII-S2P
Smc3
H3K4me3
H3K27me3
H3K9me2
Log2-fold enrichment
Density classes
A compartment
B compartment
e
A compartment
B compartment
Chromatin volume / compartment volume
Density classes

Extended Data Figure 6 | Functional marker distribution in whole mouse and human cell lines and macro-compartments. a, Bar plots of the log-2 fold over/under representation of each marker analysed in each of the segmented chromatin classes for G1 relative to chromatin class volume. Number of cells = 433. **b**, **c**, Representative selection of markers in mouse C127 mammary epithelial cells show the same zonation pattern with the same antibodies in human HCT116 colon carcinoma cells (b) and HeLa cells (c), suggesting chromatin accessibility as a universal regulator of epigenetic zonation. Number of cells: C127 = 170, HCT116 =70, HeLa = 41. **d**, **e,** Bar plots of the over/under representation of representative marker in each of the segmented G1 macro-scale A/B chromatin compartments showing a relatively conserved zonation pattern between active and repressive markers despite the different composition of chromatin density in either A or B regions (e). Plots show average log-2 value, error bars indicate 95% confidence interval. Number of cells = 170.

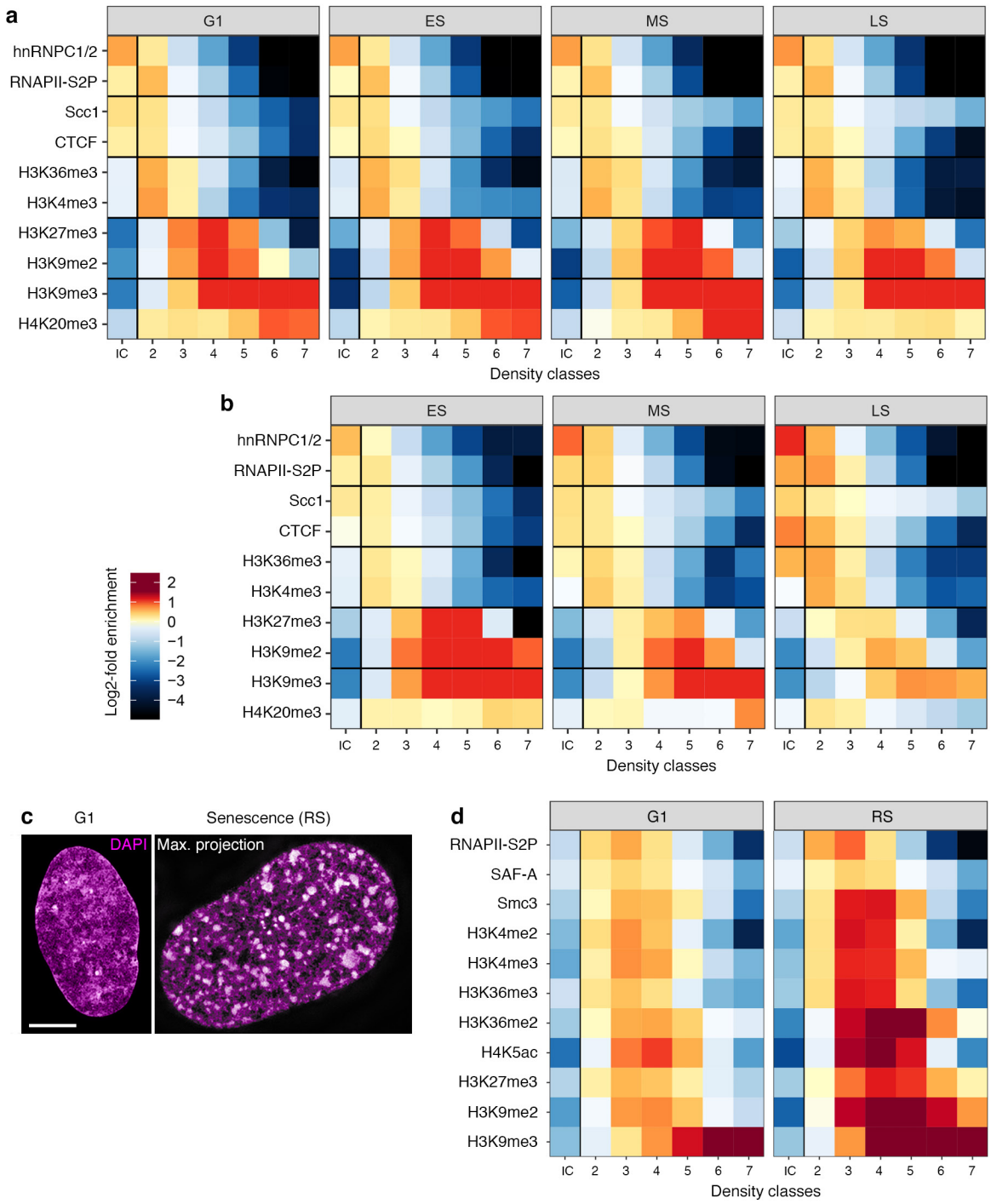

Extended Data Figure 6 | Functional marker distribution in different S-phase stages of mouse C127 mammary epithelial cells and in cycling and senescent human IMR-90 myofibroblast cells. a, Heatmaps of enrichment or depletion of IF signals relative to random (plotted in log2-fold change) per chromatin density class in the whole nuclear volume or EdU-submask (**b**). Number of cells: G1 =320, ES = 225, MS = 227, LS = 230. **c**. Super resolution imaging of DAPI-stained chromatin in G1 or replicative senescent (RS) IMR90 nucleus showing the presence of senescence-associated heterochromatin foci (SAHF). **d**. Heatmaps of enrichment or depletion of IF signals relative to random (plotted in log2-fold change) per chromatin density class in G1 or RS IMR90 cells. G1 = 208 cells, RS = 211 cells.

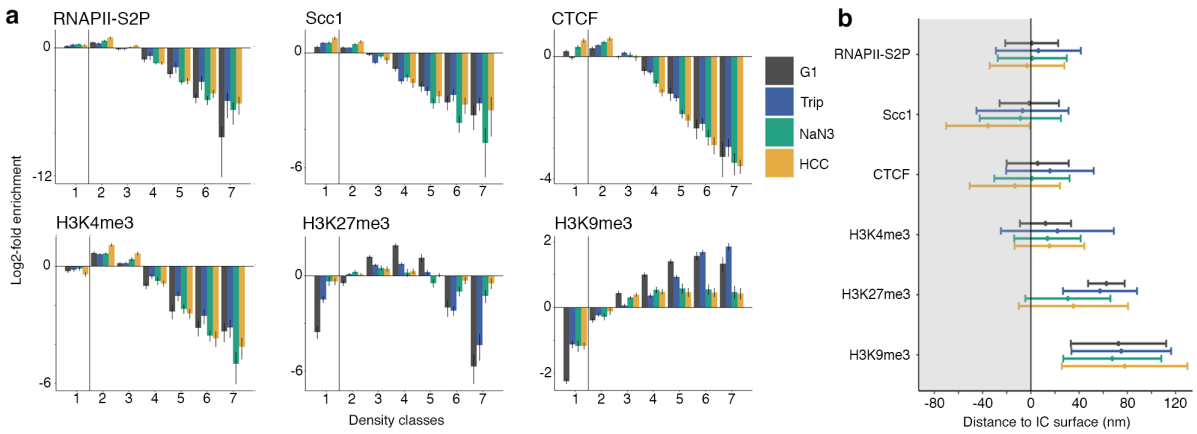

Extended Data Figure 8 | Functional marker distribution upon biophysical or transcriptional perturbation. a, Bar plots of the over/under representation of each histone PTM analysed in each of the segmented chromatin classes for G1, biophysical compaction (NaN_3 or HCC) or transcription initiation inhibition (Trip). Plots show average log-2 value, error bars indicate 95% confidence interval. **b**, Distance (nm) to the chromatin-IC boundary from a representative subset of markers in Figure 2b comparing G1, NaN_3, HCC and Trip. Number of cells: G1 = 210, NaN_3 = 120, HCC =120, Trip=123.

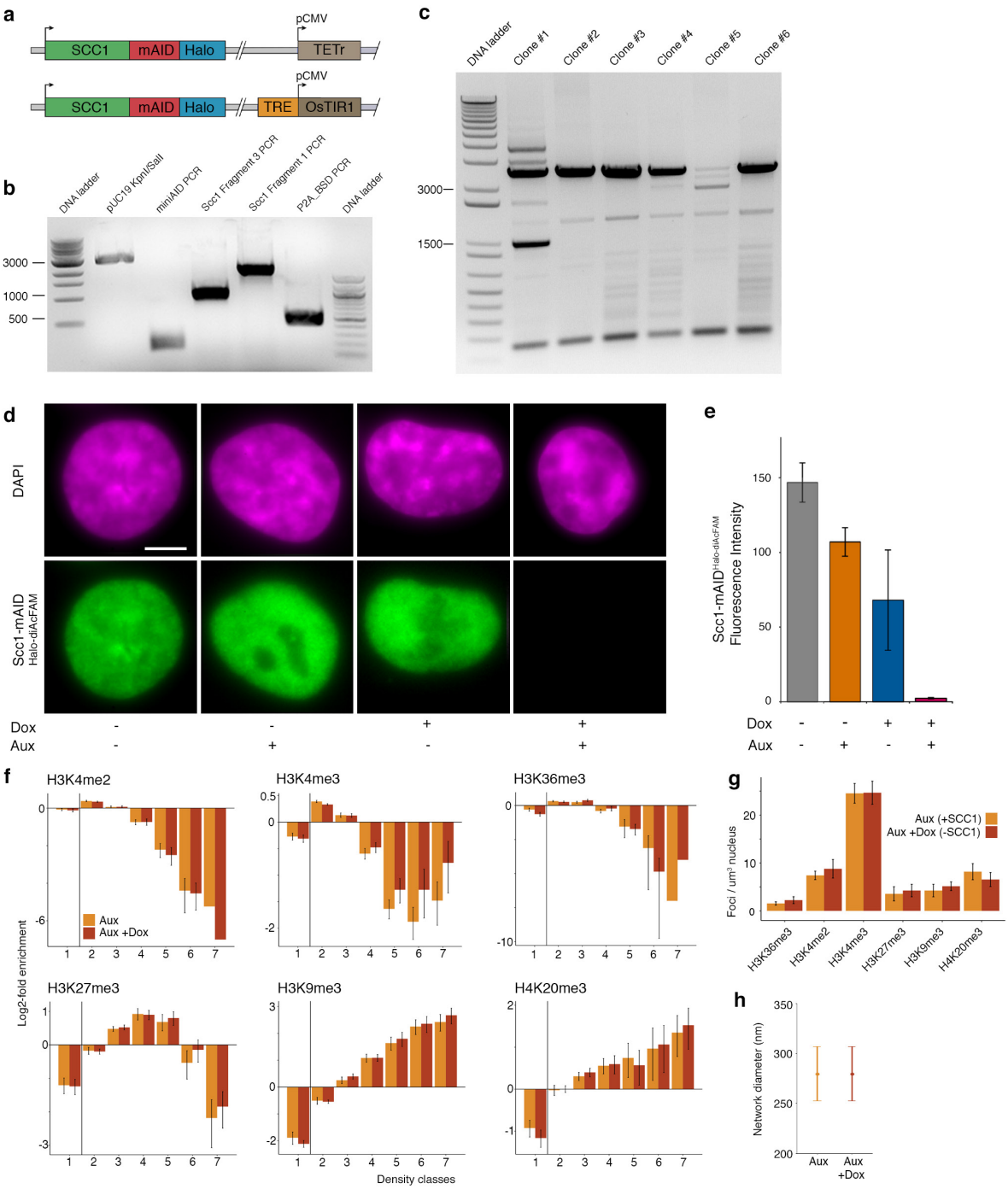

Extended Data Figure 8 | Generation of the HCT116 Tet-OsTIR1 Scc1-mAID-Halo cell line and functional marker distribution for Scc1 ablation. **a**, Schematic overview of the genomic construct. Both endogenous Scc1 alleles are tagged with an auxin-inducible degron (mAID) and a HaloTag. In the presence of doxycycline, the TIR platform is activated by the Tet system to produce an E3 ligase. The E3 ligase will induce proteosomal degradation of all mAID tagged proteins in the presence of auxin. **b**, Agarose gel of PCR amplified products required for the generation of the Scc1 NT-BSD-GSG-P2A-mAID-HaloTag construct. **c**, Screening of clones after CRISPR-Cas9 mediated incorporation of the construct described in **a** and **b**. Wildtype Scc1 has an expected size of ~1500 bp and modified Scc1 has an

expected size of ~3800 bp. Clone #1 shows is heterozygous for the integration whereas clone #2,3,4,6 are homozygous. For this study, clone #2 was expanded. **d**, Representative widefield fluorescent DAPI and SCC1-mAID signal after mock induction, 2 h auxin (aux), 16 h doxycycline (dox), or both 2 h aux and 16 h dox (left to right respectively). Scale bar: 5 μm. **e**, Quantification of the fluorescent intensity in the different conditions of (d). N = 10 cells per condition (error bars = SD). **f**, Bar plots of the over/under representation of each histone PTM analysed in each of the segmented chromatin classes with or without Scc1 ablation (6h aux +/- 16 h dox) in HCT116 cells. Plots show average log-2 value, error bars indicate 95% confidence interval. **g**, Quantification of the mean number of foci detected for each condition shows no significant change (error bars = SD). **h**, Quantification of the filament dimensions shows no significant change between Scc1 positive or depleted conditions (bars= 95% confidence interval). For analyses **f-h** number of cells: Aux = 80, Aux + Dox = 104.

Extended Data Table 1 | Average number of foci analysed per marker

	C127			
Marker	**G1 (ΣN=433)**	**ES (ΣN=225)**	**MS (ΣN=227)**	**LS (ΣN=230)**
CTCF	7130 ± 2025 (40)	4784 ± 1699 (30)	4052 ± 2732 (30)	3878 ± 3360 (30)
H3K27me3	2590 ± 1500 (40)	1906 ± 1727 (20)	1940 ± 1734 (18)	1949 ± 1576 (20)
H3K36me2	3260 ± 1993 (20)	-	-	-
H3K36me3	1323 ± 515 (40)	2822 ± 1396 (30)	2541 ± 1153 (30)	392 ± 356 (30)
H3K4me2	2708 ± 1089 (20)	-	-	-
H3K4me3	5556 ± 1207 (40)	3692 ± 1777 (30)	2781 ± 2416 (29)	3104 ± 2778 (30)
H3K9me2	4787 ± 988 (30)	1169 ± 535 (15)	2753 ± 1405 (20)	2548 ± 1867 (20)
H3K9me3	1908 ± 1603 (30)	688 ± 230 (20)	809 ± 412 (20)	664 ± 229 (20)
H4K20me3	4523 ± 356 (20)	2598 ± 583 (20)	1959 ± 1196 (20)	2344 ± 392 (20)
H4K5ac	5177 ± 1527 (20)	-	-	-
hnRNPC1/2	4625 ± 781 (20)	1224 ± 423 (20)	865 ± 174 (20)	614 ± 220 (20)
Nascent RNA	2797 ± 1124 (13)	-	-	-
RNAPII-S2P	5027 ± 1319 (40)	2830 ± 1860 (30)	2698 ± 2530 (30)	3019 ± 2360 (30)
SAF-A	4655 ± 1821 (20)	-	-	-
Scc1	1272 ± 391 (20)	981 ± 193 (10)	991 ± 102 (10)	1146 ± 244 (10)
Smc3	615 ± 263 (20)	-	-	-

	C127			HeLa
Marker	**NaN_3 (ΣN=120)**	**Hyper-os (ΣN=120)**	**Trip (ΣN=123)**	**G1 (ΣN=41)**
CTCF	4097 ± 2491 (20)	8032 ± 1690 (20)	10717 ± 1887 (23)	-
H3K27me3	2077 ± 840 (20)	3693 ± 847 (20)	7259 ± 2978 (23)	-
H3K4me3	5814 ± 1832 (20)	5592 ± 933 (20)	8705 ± 1603 (11)	7341 ± 1785 (10)
H3K9me3	2726 ± 610 (20)	1505 ± 362 (20)	4122 ± 2250 (23)	5837 ± 525 (11)
RNAPII-S2P	6263 ± 1277 (20)	6161 ± 1157 (20)	2275 ± 900 (20)	3719 ± 819 (10)
Scc1	1272 ± 358 (20)	1046 ± 749 (20)	4971 ± 3055 (23)	-
hnRNPC1/2	-	-	-	7531 ± 1463 (10)

	HCT116 (Scc1-mAID)		IMR90	
Marker	**6hr Aux (ΣN=80)**	**6hr Aux + 16hr Dox (ΣN=104)**	**G1 (ΣN=208)**	**RS (ΣN=211)**
H3K27me3	1077 ± 516 (20)	1379 ± 407 (30)	2253 ± 418 (20)	7591 ± 3657 (19)
H3K36me2	-	-	3253 ± 2056 (20)	6416 ± 2500 (20)
H3K36me3	551 ± 138 (10)	790 ± 263 (12)	843 ± 396 (20)	2526 ± 1415 (19)
H3K4me2	2620 ± 413 (10)	3063 ± 412 (12)	4011 ± 656 (19)	6298 ± 2329 (18)
H3K4me3	7409 ± 1252 (20)	8155 ± 1420 (30)	4424 ± 555 (20)	9546 ± 5158 (20)
H3K9me2	-	-	3868 ± 628 (20)	7946 ± 2605 (20)
H3K9me3	1182 ± 204 (10)	1771 ± 174 (10)	2134 ± 490 (20)	3714 ± 2007 (19)
H4K20me3	2316 ± 387 (10)	2246 ± 272 (10)	-	-
H4K5ac	-	-	3565 ± 512 (10)	8901 ± 3504 (18)
RNAPII-S2P	-	-	3979 ± 715 (20)	7467 ± 4002 (19)
SAF-A	-	-	3823 ± 1992 (19)	11051 ± 5092 (20)
Smc3	-	-	1159 ± 287 (20)	2000 ± 1226 (19)

Average number of IF spots ± SD of each marker per cell for (N) number of cells in each condition after high stringency filtering to avoid false positives. Cell cycle stages are abbreviated to ES, MS and LS for earl, mid and late S phase, and RS for senescence. To maintain consistency, the same mammalian antibodies were used throughout this study, however the affinity of some antibodies is greater or decreased in either mouse (C127) or human (HCT116, IMR90) cells. The numbers for IMR90 cells in RS are consistently at least double that of G1as these are predominantly binuclear due to defective cytokinesis.

METHODS

Plasmids

pSpCas9(BB)−2A-Puro V2.0 targeting SCC1 (PX459 SCC1(Hs)) was a gift from James Rhodes[50]. A poly Glycine-Serine linker, Blasticidin resistance gene (BSD), GSG-P2A, mini auxin-inducible degron (mAID) and HaloTag were cloned between the KpnI and SalI site of a pUC19 vector by Gibson Assembly (NEB #cat E2611). The pUC19 CT-BSD_GSG_P2A-mAID-HaloTag was cloned between two 1 kb homology arms at the 3' of Scc1 to generate pUC19 Scc1 CT-BSD-GSG-P2A-mAID-HaloTag.

BACs

The BACs used for FISH labelling of a single TAD were a gift from E. Heard[19]. They correspond to X chromosome "TAD H" characterized between genomic loci 102325818 and 102998976 (673158 bp). The four BACs required to cover this region are: 6-RP24-217I10 (102302874:102459532), 7-RP23-469A2 (102465652:102651023), 8-RP23-331L13 (102648562:102834423) and 9-RP24-396M14 (102804354:102976347) spanning a total length of 673473 bp. The 315bp difference between BACs coverage and TAD boundary calling is considered negligible over the 673kb total (<0.05% error). BAC probes were directly labelled by nick translation using CF-594 (Biotium).

Cell culture

Mouse mammary gland C127 and human cervical cancer HeLa H2B-GFP cells were grown in Dulbecco's Modified Eagle Medium (DMEM) supplemented with 10% FBS, 1% penicillin and streptomycin. Human colon carcinoma HCT116 Tet-OsTIR1 cells were cultivated in McCoy's 5A medium supplemented with 10% FBS, 2 mM L glutamine and 1% penicillin and streptomycin. Human lung fibroblast IMR-90 cells were grown in Dulbecco's Modified Eagle Medium (DMEM) supplemented with 10% FBS, 1% penicillin and streptomycin. Cells were incubated at 37°C, 5% CO_2 in humidified incubator. At 90% confluence cells were sub cultured by trypsinising with 0.05-0.25% Trypsin in PBS or 1x trypsin replacement solution (TrypLE express, Gibco) and passaged to a new culture dish at appropriate dilutions (1:5-1:12 every 2-3 days).

Generation of inducible Scc1 degradation system

To generate a stable HCT116 Tet-OsTIR1 Scc1-mAID-Halo cell line, the pX459 SCC1(Hs) plasmid and pUC19 Scc1 CT-BSD-GSG-P2A-mAID-HaloTag were transfected using FuGene HD (Promega #cat PRE2311). Two days post transfection, cells were grown in

blasticidin-containing McCoy's 5A medium (5 μg/mL). After 10 days, single colonies were transferred to 96-well plates and homozygous clones were screened by PCR with primers in Supplementary Table 1.

EdU, EU and BrUTP labelling and perturbation experiments

To identify cells in S-phase 10 μM 5-ethenyl-deoxyuridine (EdU) was added 15-30 min before fixation. G1 cells were identified by being negative for EdU pulse labelling and their smaller nuclear size compared to G2 cells. Identification of G1 vs RS cells in the IMR90 cell line was done using the proliferating cell marker Ki-67. G1 cells were Ki67-positve (and EdU-negative) versus G2 Ki67-negative.

For bulk RNA labelling 1 mM EU was added 60-90 min before fixation. To label nascent RNA a 10 min BrUTP pulse labelling was performed by scratch transcription labelling approach as described[51].

For biophysical chromatin perturbation cells were incubated for 10 min before fixation and immunostaining with 50 mM of NaN_3 or 200 µl of 10xPBS (to expose cells to hyperosmotic conditions) added to growth medium. For transcriptional inhibition, cells were incubated with 1 μM Triptolide (Sigma-Aldrich) for 90 min prior to fixation; treatment leads to a strong reduction in bulk RNA signal. To Auxin induced Scc1-degradation, HCT116 cells were cultivated in the presence of 5 μg/mL doxycycline (Sigma, D9891) and 500 nM auxin (Sigma, cat# I5148) for 16 h and 6 h, respectively.

RASER-FISH and probe labelling

RASER-FISH maintains nuclear fine-scale structure by replacing heat denaturation with exonuclease III digestion of one of the two DNA strands after UV-induced generation of nicks, and is suitable for high- and super-resolution imaging analysis[34]. Briefly, cells were labelled overnight with a BrdU/BrdC mix (3:1) at final conc. of 10 μM. Cells were fixed in 2% formaldehyde for 15 min and permeabilised in 0.2% Triton X-100/PBS (vol/vol) for 10 min. Cells were incubated with DAPI (0.5 μg/mL in PBS), exposed to 254 nm wavelength UV light for 15 min, then treated with Exonuclease III (NEB) at final conc. 5 U/μL at 37°C for 15 min. Labelled probes (100 ng each) were denatured in hybridization mix at 90°C for 5 min and pre-annealed at 37°C for 20 min. Coverslips were hybridized with prepared probes at 42°C.

Immunofluorescence (IF) labelling

IF labelling was performed as described in detail[36,52]. The antibodies used in this investigation are listed in Supplementary Table 2. One day before labelling, cells were grown

on 22x22 mm #1.5H high precision 170 µm ± 5 µm coverslips (Marienfeld Superior). HCT116 Tet-OsTIR1 Scc1-mAID-Halo cells were fluorescently tagged by incubating with 50 nM HaloTag diAcFAM (Promega, cat# G8272) or 500 nM HaloTag JF488 for 30 min. HCT116 cells were incubated in HaloTag-free medium for 30 min to remove residual ligand. Prior to fixation, cells were washed twice with PBS. Cells were fixed in 2% formaldehyde/PBS (Sigma, #cat F8775) for 10 min, washed with 0.02% Tween-20/PBS (PBST) and permeabilized in 0.1-0.5% Triton-X-100/PBS. Coverslips were washed three times with PBST and incubated for 30 min in MaxBlock (Active motif, cat# 15252). Cells were stained with primary antibodies against the protein of interest, washed three times with PBST and stained with fluorescently labelled secondary antibodies. After washing, cells were post-fixed in 4% formaldehyde/PBS for 10 min and counterstained using 1-2 mg/μL 4',6-diamidino-2-phenylindole (DAPI) for 10 min. Coverslips were mounted in non-hardening Vectashield (Vector Laboratories, cat# H-1000) and stored at 4°C.

Structured illumination microscopy (SIM) image acquisition, reconstruction and quality control

3D-SIM images were acquired with a DeltaVision OMX V3 Blaze system (GE Healthcare) equipped with a 60x/1.42 NA PlanApo oil immersion objective (Olympus), pco.edge 5.5 sCMOS cameras (PCO) and 405, 488, 593 and 640 nm lasers. For fixed cell imaging, 3D image stacks were acquired over the whole cell volume in z and with 15 raw images per plane (five phases, three angles). Spherical aberration was minimized using immersion oil with RI 1.514 for sample acquisition. The raw data was computationally reconstructed with SoftWoRx 6.5.2 (GE Healthcare) using channel-specific OTFs recorded using immersion oil with RI 1.512, and Wiener filter settings between 0.002-0.006 to generate 3D stacks of 115 nm (488 nm) or 130 nm (592 nm) lateral and approximately 350 nm axial resolution. All SIM data was routinely and meticulously quality controlled for effective resolution and absence of artifacts using SIMcheck[53], an open-source Image J plugin to assess SIM image quality via modulation contrast-to-noise ratio, spherical aberration mismatch, reconstructed Fourier plot and reconstructed intensity histogram values. (for more details see [52]). Multi-channel acquisitions were aligned in 3D using Chromagnon software[54] based 3D-SIM acquisitions of multi-colour EdU labelled C127 cells[36]. 3D-SIM imaging of DAPI or SYTOX Green stained DNA typically provides a high-contrasted spatial representation of chromatin distribution with a lateral resolution of 100-110 nm.

For live cell 3D-SIM, HeLa H2B-GFP cells were seeded in a 35 mm μ-Dish, high Glass Bottom (Ibidi) using phenol red free DMEM medium supplemented with 10 μM

HEPES. Live cell imaging was performed at 5% CO_2 supply and keeping sample at 37°C using stage and objective heater) we recorded for each timepoint a central region over 7 z-positions with 125 nm distance covering a total range of 0.75 μm and totalling 105 raw images (5 phases x 3 angles x 7 z-positions). Using 10 ms exposure time and 31% laser transmission of the 488 nm laser a frame rate of down to 0.5 Hz could be achieved, and typically 12 time points could be recorded until the photon budget was exhausted due to photobleaching.

3D STED micrographs of SYTOX green stained C127 cells were acquired on a Leica TCS SP8 STED 3X system equipped with a 100x/1.4 NA oil objective using 50% of depletion energy for axial resolution increase resulting in a nominal resolution of ~100 nm in x-y and ~200 nm in z-direction. To compensate for low dynamic range and SNR raw STED data was subjected to a constrained iterative 3D deconvolution using Huygens software (SVI). 3D STED achieves comparable or slightly better resolution than 3D-SIM for high labelling density samples such as chromatin at the expense of slower acquisition speed, a major drawback in a high-throughput analysis investigation.

Quality validation

3D-SIM imaging and subsequent quantitative analyses is susceptible to artefacts[52]. For instance, bulk labelling of densely packed chromatin inside mammalian nuclei of several μm depth entails high-levels of out-of-focus blur, which reduces the contrast of illumination stripe modulation and thus the ability to recover high frequency (i.e., super-resolution) structure information. We therefore carefully assessed and optimized system performance as well as raw and reconstructed data quality using SIMcheck ImageJ plugin[53] (Extended Data Fig. 1a). To exclude potential false positive calls, we used the *Modulation Contrast-to-Noise-Ratio (MCNR) map* macro of SIMcheck, which generates a metric of local stripe contrast in different regions of the raw data and directly correlates with the level of high-frequency information content in the reconstructed data[52]. Only IF spot signals whose underlying MCNR values exceed a stringent quality threshold were considered while localisations with low underlying MCNR were discarded to exclude any SIM signal which falls below reconstruction confidence in all datasets before feeding these to the analysis pipeline (Supplementary Fig. 1). We noted that most nuclear spots (dependent on the antibody between a few hundred to several thousand per nucleus) were in the size range of 3D-SIM resolution limited point signal, and their intensities were similar to seldom extranuclear spots from non-specifically bound primary-secondary antibody complexes (concentrating less than

10 dyes). We therefore conclude that nuclear signals predominantly represent the binding of a primary-secondary antibody complex to a single epitope.

Cha*i*N - pipeline for high-content analysis of the 3D epigenome

Cha*i*N (for Chain high-throughput analysis of the *in situ* Nucleome) describes a pipeline of scripts for the automated high-throughput analyses in this investigation (Extended Data Fig. 5). In brief, the counterstain/chromatin channel is used to generate (1) a nuclear mask and (2) segment chromatin topology into 7 intensity/density classes using an R script that is expanding on a Hidden Markov model[55]. Based on the output of Cha*i*N, we can quantitatively assess multiple parameters, such as the overall volume of the chromatin filament (combined classes 2-7, Extended Data Fig. 1d, e) versus IC (class 1), its 3D surface, and the surface-to-volume-ratio. The volume of the segmented chromatin fraction occupied approximately two thirds of the total nuclear volume (~400 of 600 μm^3 in G1 C127 cells).

The IF signals for markers are thresholded by intensity using the Otsu algorithm, with all non-foci voxels replaced by zeros. The complement of this is image is segmented by a 3D watershed algorithm and the 3D centroid coordinates extracted from each segmented region's centre of mass after weighting by local pixel intensities. To filter out potential false positive localizations using a local modulation-contrast-to-noise-ratio (MCNR) threshold to avoid potential artefacts skewing the statistical output[52,53] (Supplementary Fig. 1). The quality controlled and filtered centroid positions were then related to the chromatin-interchromatin volume in two ways: The spot positions falling into each of the 7 segmented classes were counted, normalized to the respective class size and their relative enrichment (or depletion) displayed in a heat map on a log 2-fold scale.

Indexing IF coordinates on the segmented chromatin yields their enrichment/depletion profiles at different chromatin densities normalized to the volumes of each chromatin density class. Segmentation of the 3D surface between class 1 and all other classes allows for Euclidian distance calculation between the IF coordinates and the nearest filament surface voxel. The segmented surface can also be normalized to the volume of total chromatin to obtain a surface area to volume ratio of the filament.

Finally, by sampling the distance between the surface and random coordinates, assuming a tubular based structure, it is possible to estimate the average radius and diameter of the filament (Extended Data Fig. 3). The average radius R can be sub divided into a smaller radius "r" which encompasses the inner half of the volume of the tube (and therefore half the area of the cross-section) and δ, the difference between r and R. First, we

define two circles (A1 with radius r+δ and A2 with radius r) of which the area of A1 is twice the area of A2. Based on simple calculus we can determine that R = 3.4142 δ. Second, if we randomly distribute points over the entire tube, 50% of the points will be located within circle A2 whereas the other 50% will located in A2 - A1. Third, if we calculate the minimum distance of the points in the circle of A2 - A1 we can define the value of δ, which is 50% of the area under the frequency curve of the right histogram. Lastly, by multiplying this value with 3.4142, we can estimate the average radius of tubular chromatin filaments in cell nuclei. We note, the total number of discrete segmentation bins used in this analysis is arbitrary, with the sole criterion to group all non-detectable chromatin voxels as one class (class 1, IC). It is therefore an important validation of this approach to observe that, on average, elongating RNAP (RNAPII-S2P) primarily localizes at the chromatin-IC interface or within +/- 20 nm of this feature with 95% confidence, suggesting that the *in silico* determined boundary between IC or chromatin in this analysis is true to an underlying biological demarcation.

Quantitative evaluation of chromatin dynamics

Spatial correlation dynamics of chromatin was estimated by using Dense Flow reConstruction and Correlation (DFCC)[31]. Briefly, DFCC was applied to estimate the 2D apparent motion of two consecutive images in an image sequence (N-1); the direction and magnitude of flow fields of each pixel (size = 41 nm) were estimated for H2B-GFP over 20 image series and with time interval of 2 s. Then, spatial auto-correlation of scalar fields representing motion direction was calculated by Fast Fourier Transform algorithms and is given by

$$r(\Delta x, \Delta y) = \frac{\mathcal{F}^{-1}[\mathcal{F}(\gamma) \cdot \mathcal{F}^{*}(\gamma)]}{\langle\gamma\rangle\langle\gamma\rangle},$$

where $\mathcal{F}(\cdot)$, $\mathcal{F}^{-1}(\cdot)$, and $\mathcal{F}^{*}(\cdot)$ are the Fourier transformation, inverse Fourier transformation and the complex conjugate of the Fourier transformation, respectively. Correlation corves for different time lags were fitted using the Whittle-Màtern model, and therefore, the correlation length and smoothness parameters extracted for each time lags.

Hi-D method was applied to estimate the biophysical properties of chromatin motion in living Hela cells at pixel resolution (41 nm)[49].

Mean square displacement (MSD) curves were plotted over time lags representing the trajectories of chromatin in the entire nucleus. Then, Bayesian inference approach applied to test the below five principle models for each MSD curves in order to classify types of motion. Fitting of the MSD derived from trajectories can be expressed for anomalous diffusion (α), free diffusion constant (D), directed motion (V) or a combination thereof. The

value of each biophysical parameter extracted by this fitting is then mapped in 2D colour map, also five principal models are shown as a coloured map directly on the nucleus (Extended Data Fig. 2b).

$$MSD_D(\tau) = 4D\tau + o$$

$$MSD_{DA}(\tau) = 4D\tau^{\alpha} + o$$

$$MSD_V(\tau) = v^2\tau^2 + o$$

$$MSD_{DV}(\tau) = 4D\tau + v^2\tau^2 + o$$

$$MSD_{DAV}(\tau) = 4D\tau^{\alpha} + v^2\tau^2 + o$$

Where D: Free diffusion; DA: Anomalous diffusion; V: Drift velocity of flow fields; DV: Free diffusion + drift; DAV Anomalous diffusion + drift; τ: Time interval.

Data and Code Availability

All data, parameters and scripts used are available for reproducing the results of this investigation. Raw and reconstructed 3D SIM images, with reconstruction and alignment parameters can be found in the Open Microscopy Environment server: OMERO. The programs required to run all scripts for image analysis are: ImageJ (Fiji distribution with SIMcheck), R and Octave. Scripts for ChaiN and the DFCC analysis are available in the following GitHub repositories: https://github.com/ezemiron/Chain, https://github.com/romanbarth/DFCC.